Rapid synthesis of bismuth-organic frameworks as selective antimicrobial materials against microbial biofilms

Regina Huang [a], Zhiwen Zhou [b], Xinmiao Lan [c], Fung Kit Tang [d], Tianfan Cheng [a], Hongzhe Sun [e], Ken Cham-Fai Leung [d], Xuan Li [a,**], Lijian Jin [a,*]

[a] *Faculty of Dentistry, The University of Hong Kong, Hong Kong SAR, China*
[b] *Department of Mechanical Engineering, Faculty of Engineering, The University of Hong Kong, Hong Kong SAR, China*
[c] *School of Pharmaceutical Sciences, Capital Medical University, Beijing, China*
[d] *Department of Chemistry, State Key Laboratory of Environmental and Biological Analysis, The Hong Kong Baptist University, Hong Kong SAR, China*
[e] *Department of Chemistry, State Key Laboratory of Synthetic Chemistry, CAS-HKU Joint Laboratory of Metallomics on Health and Environment, The University of Hong Kong, Hong Kong SAR, China*

ARTICLE INFO

ABSTRACT

Antibiotic resistance is a global public health threat, and urgent actions should be undertaken for developing alternative antimicrobial strategies and approaches. Notably, bismuth drugs exhibit potent antimicrobial effects on various pathogens and promising efficacy in tackling SARS-CoV-2 and related infections. As such, bismuth-based materials could precisely combat pathogenic bacteria and effectively treat the resultant infections and inflammatory diseases through a controlled release of Bi ions for targeted drug delivery. Currently, it is a great challenge to rapidly and massively manufacture bismuth-based particles, and yet there are no reports on effectively constructing such porous antimicrobial-loaded particles. Herein, we have developed two rapid approaches (*i.e.,* ultrasound-assisted and agitation-free methods) to synthesizing bismuth-based materials with ellipsoid- (Ellipsoids) and rod-like (Rods) morphologies respectively, and fully characterized physicochemical properties. Rods with a porous structure were confirmed as bismuth metal-organic frameworks (Bi-MOF) and aligned with the crystalline structure of CAU-17. Importantly, the formation of Rods was a 'two-step' crystallization process of growing almond-flake-like units followed by stacking into the rod-like structure. The size of Bi-MOF was precisely controlled from micro-to nano-scales by varying concentrations of metal ions and their ratio to the ligand. Moreover, both Ellipsoids and Rods showed excellent biocompatibility with human gingival fibroblasts and potent antimicrobial effects on the Gram-negative oral pathogens including *Aggregatibacter actinomycetemcomitans*, *Porphyromonas gingivalis* and *Fusobacterium nucleatum*. Both Ellipsoids and Rods at 50 μg/mL could disrupt the bacterial membranes, and particularly eliminate *P. gingivalis* biofilms. This study demonstrates highly efficient and facile approaches to synthesizing bismuth-based particles. Our work could enrich the administration modalities of metallic drugs for promising antibiotic-free healthcare.

1. Introduction

Antimicrobial resistance as a global public health crisis accounts for a huge healthcare burden with massive socio-economic impacts [1]. It is highly urgent to develop alternative antimicrobial strategies and approaches to tackling this serious issue. Recently, both organic- and inorganic-based materials have been increasingly used to combat the crisis, such as molybdenum disulfide for releasing near-infrared light--induced nitric oxide and cobalt-doped nickel oxide nanoparticles for enhancing the catalytic effects of reactive oxygen species on bacterial biofilms [2–11]. It is noteworthy that bismuth as a relatively environmental-friendly heavy metal has been used for catalysis, energy storage and biomedicines [12–15]. Over the years, bismuth has acted as effective antibiotic adjuvants against *Helicobacter pylori*-induced gastrointestinal infections [16]. Additionally, it can restore the sensitivity of bacteria with drug-resistant genes to antibiotics [17,18]. Our recent work shows that bismuth drugs with metronidazole synergistically eradicate the noxious persisters of the keystone periodontopathogen -

Porphyromonas gingivalis (*Pg*), and yet the bismuth drugs alone could reverse *Pg*-triggered disturbance of immunoinflammatory responses in host cells [19,20]. Importantly, the less cytotoxic ranitidine bismuth citrate has been confirmed as a potential therapeutic agent for treating SARS-CoV-2 infections [21,22]. Therefore, bismuth drugs or bismuth-based materials with selective inhibitory effects on various Gram-negative pathogens hold great potentials to be utilized for antibiotic-free treatments. However, it remains a great challenge to rapidly and massively manufacture bismuth-based particles, and currently there are no reports on constructing such porous antimicrobial-loaded particles.

Bismuth-based materials, owing to the high affinity of bismuth towards sulfur, nitrogen and oxygen, have been constructed into diverse forms (*e.g.*, complexes, oxyhalides and composite oxides) *via* various approaches such as conventional, hydrothermal, sonochemical and microwave-assisted methods [15,23–27]. Remarkably, metal-organic frameworks (MOFs), a group of hybrid crystalline materials composed of metal ions and organic ligands, demonstrate high surface area and ultrahigh porosity [28–34]. As such, MOFs are promising candidates for various applications, including gas storage and separation, sensing, catalysis, proton conduction, drug delivery and antimicrobial coating agents [34–39]. The Bi^{3+}-coordinated MOFs (Bi-MOFs), compared to other MOF types, possess potent antimicrobial activities and may serve as potential drug carriers or antimicrobial agents [40–43]. However, it is noted that only four microporous Bi-MOFs (CAU-7, CAU-17, CAU-35 and NOTT-220) have been reported so far [44]. Amongst, CAU-17 can be successfully synthesized with Bi^{3+} and trimesic acid through hydrothermal, sonochemical and microwave-assisted methods [30,31,36]. Nevertheless, mass production of CAU-17 is still time-consuming, device-dependent (*e.g.*, ultrasonic probes, laboratory-used oven and microwave) and condition-restricted (*e.g.*, high temperature and pressure). Thus, it remains a great challenge to rapidly and massively manufacture Bi-MOFs in ambient environments using an eco-friendly method.

Here, we present novel approaches to constructing two featured types of bismuth-based particles with detailed characterizations. We confirmed one of the forms to be CAU-17 by its crystalline structure (Scheme 1a). Notably, the agitation-free method for synthesizing Bi-MOFs has been thoroughly studied to identify the crystallization process and the influential factors on the structure and morphology of MOF (Scheme 1b). Afterward, the antibacterial and anti-biofilm effects of the as-synthesized bismuth-based particles were assessed on eight representative Gram-positive and Gram-negative pathogens, namely *Streptococcus mutans* (*Sm*), *Streptococcus sobrinus* (*Ss*), *Enterococcus faecalis* (*Ef*), methicillin-resistant *Staphylococcus aureus* (MRSA), *Pseudomonas aeruginosa* (*Pa*),
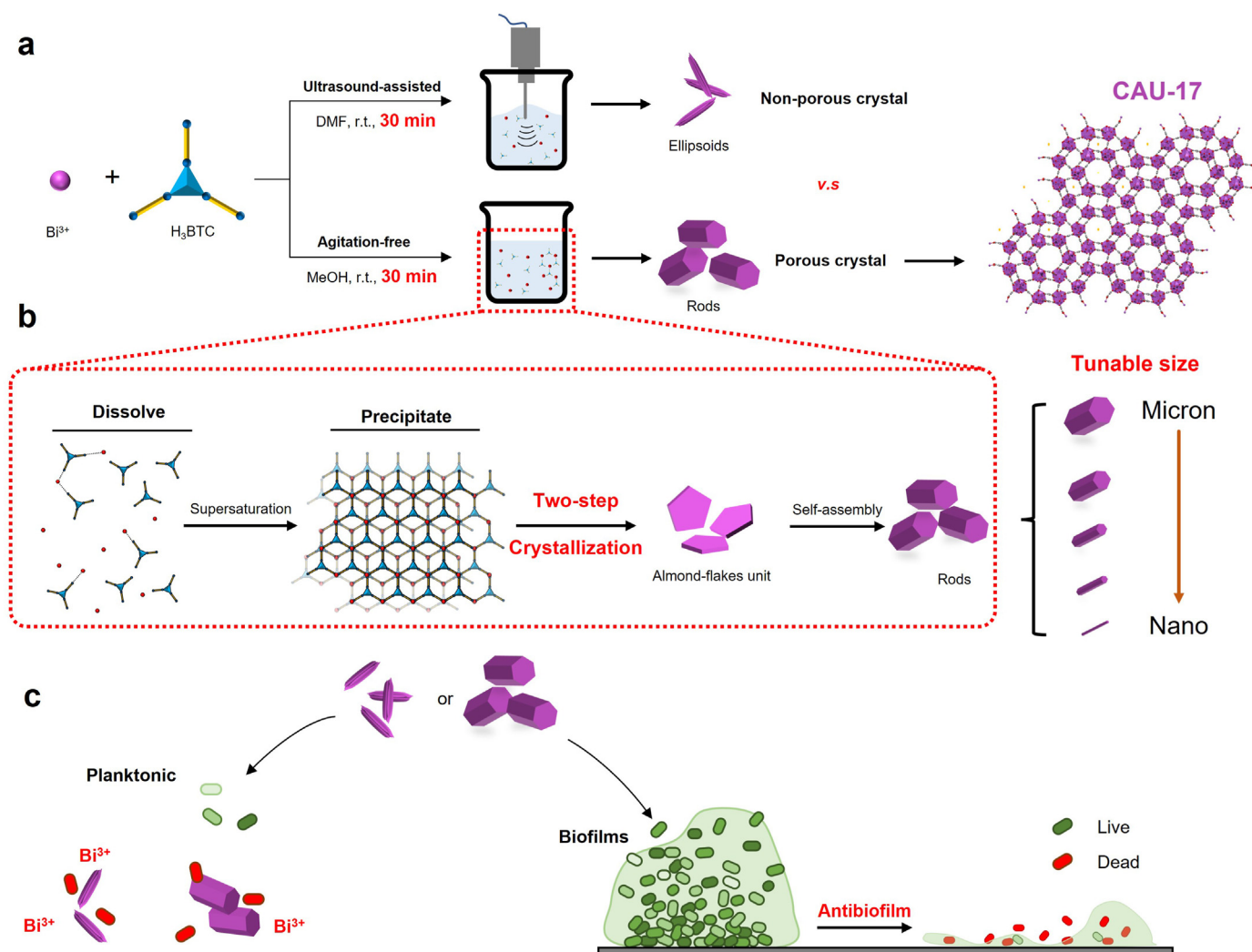
Scheme 1. Schematic illustration of the synthesis, crystallization mechanism and antibacterial effects of bismuth particles. a) Two approaches were developed for synthesizing bismuth-based particles in 30 min, and the porous one with rod-like shape (Rods) was characterized as Bi-MOFs with the crystalline structure of CAU-17; b) the formation of Rods in methanol was a 'two-step' crystallization process, and the size of Rods was tunable from micron-to nanometer; c) the as-synthesized bismuth particles could disrupt the membrane of selected Gram-negative bacteria and show potent antibiofilm effects *in vitro*.

Aggregatibacter actinomycetemcomitans (*Aa*), *P. gingivalis* (*Pg*) and *Fusobacterium nucleatum* (*Fn*) (Scheme 1c). The cytotoxicity of the Bi particles was assessed on human gingival fibroblasts. Particularly, the bismuth-based materials have comparable antimicrobial effects as the commercialized bismuth drug – colloidal bismuth subcitrate (CBS). Our current findings may shed light on providing more diverse and facile approaches to synthesizing the porous and non-porous bismuth particles, while simultaneously enriching the administration modalities of metallic drugs and their promising applications in antibiotic-free healthcare.

2. Material and methods

2.1. Chemicals

Trimesic acid (H$_3$BTC), bismuth (III) nitrate pentahydrate (Bi(NO$_3$)$_3$·5H$_2$O) and tetrazolium salt dye (2,3,5-triphenyl tetrazolium chloride, TTC) were obtained from Meryer (Shanghai, China). Sodium acetate (NaOAc) was ordered from Fisons (Loughborough, UK). Methanol (MeOH) and penicillin G (PEN) were obtained from Merck (Darmstadt, Germany), and *N,N*-dimethylformamide (DMF) and amoxicillin (AMX) were from Sigma-Aldrich (St. Louis, USA). Acetone was ordered from RCI Labscan (Bangkok, Thailand). Colloidal bismuth subcitrate (CBS) was received from Lizon Pharmaceutical Limited (China) and diluted with sterile deionized water (DI H$_2$O) to 100 mM before use.

2.2. Synthesis of Bi-based materials

Ellipsoid-like bismuth particles (Ellipsoids) were prepared according to the report with some modifications [45]. First, 336 mg (1.6 mmol) of H$_3$BTC and 78 mg (0.16 mmol) of Bi(NO$_3$)$_3$·5H$_2$O were completely dissolved in 30 mL of DMF to get a clear solution. Subsequently, 10 mg (0.76 mmol) of NaOAc as modulator in 1 mL of MeOH were added dropwise to the solution and sonicated (20 kHz, 38% amplitude for 3 s followed by pausing for 7 s; Sonics & Materials Inc., Danbury, USA) for 10 min. After the appearance of white precipitates, the reaction was terminated and settled at room temperature. The particles were washed with MeOH and collected by centrifugation at 8000 rpm (High-Speed Refrigerated Centrifuge CR 22 N, Hitachi Ltd., Tokyo, Japan) for 3 min.

Referring to the synthesis of rod-like Bi-MOFs (Rods), 336 mg (1.6 mmol) of H$_3$BTC and 78 mg (0.16 mmol) of Bi(NO$_3$)$_3$·5H$_2$O were added into a 50 mL Flacon tube filled with 30 mL of MeOH and sonochemically dissolved using an ultrasonic bath (Branson 2200, Branson Ultrasonics Crop., Connecticut, USA) with minimal perturbation. The solution was left undisturbed at ambient temperature for recrystallization. In due time, the solution would turn from opaque to clear and maintain its transparency for the next 10 min. Thereafter, white precipitates gradually appeared in the solution and were deposited at the bottom of the tube. The particles were collected by centrifugation (8000 rpm for 3 min) followed by washing with MeOH three times.

In regard to studying the *in-situ* formation of Rods, almond flake-like bismuth particles (Almond flakes) were prepared accordingly in similar ways to Rods but with agitation or ultrasound-assisted disturbance. Both types of particles were collected every 5 min during the synthesis for a total of 90 min. The supernatant was discarded after centrifugation, and the solids were directly resuspended in acetone for electron microscopy (EM) assessment.

2.3. Characterizations of Bi-based materials

The morphology of Bi-based particles was determined by scanning electron microscope (SEM; Hitachi Ltd., Tokyo, Japan), Hitachi S-4800 field emission scanning electron microscopes (FE-SEM; Hitachi Ltd., Tokyo, Japan) and Tecnai G2 20 S-TWIN transmission electron microscopy (TEM; FEI, Hillsboro, USA) equipped with Energy Dispersive X-ray Spectrometer (EDX). TGA-6 Thermogravimetric Analyzer (TGA; Perkin Elmer, Waltham, USA) was used to assay the thermal decomposition of

the samples, whereas the surface area and pore size were measured by the nitrogen (N$_2$) adsorption-desorption isotherms at around 77 K using the ASAP 2020 M system (Micromeritics, Norcross, USA). The Nicolet Magna 550 Series II Fourier transform infrared spectroscopy (FT-IR; Nicolet Instrument, Madison, US) and Thermo Scientific K-Alpha X-ray photoelectron spectrometer (XPS) modified with monochromatic radiation AlKα source (1486.6 eV) were used to evaluate the elemental composition and states of the materials. For the crystallinity, powder X-ray diffraction (PXRD) analysis was performed using Bruker D8 Advance X-ray Diffractometer, and the results were retrieved from X Pert-Philips X-ray diffractometer equipped with monochromatized CuKα radiation (1.5406 Å, 55 kV and 40 mA).

2.4. Stability of Ellipsoids and Rods in different solutions or culture media

The particles were suspended in deionized (DI) H$_2$O, phosphate-buffered saline (PBS, pH 7.2), tryptic soy broth (TSB; 30 g/L tryptic soy broth from Difco, 5.0 g/L yeast extract from Difco and 1% hemin and vitamin K$_1$ solution) and brain heart infusion (BHI; Difco), respectively; and sampled on days 1, 2, 4, 7 and 14, followed by washing with DI H$_2$O thrice before EM assessment.

2.5. Bacterial strains and growth conditions

All bacteria strains were obtained from the American Type Culture Collection (ATCC, Manassas, USA), including *A. actinomycetemcomitans* (*Aa*; ATCC 29523), *P. gingivalis* (*Pg*; ATCC 33277), *E. faecalis* (*Ef*; ATCC 29212), *F. nucleatum* (*Fn*; ATCC 25586), *S. mutans* (*Sm*; ATCC 35668), *S. sobrinus* (*Ss*; ATCC 33478), *P. aeruginosa* (*Pa*; ATCC 27853) and methicillin-resistant *S. aureus* (MRSA; ATCC 33592). Unless otherwise specified, all strains were maintained on blood agar plates (39 g/L Columbia agar base from Difco, 5% Defibrinated Horse Blood from Hemostat and 1% hemin and vitamin K$_1$ solution) anaerobically (*Aa*, *Pg* and *Fn*)/aerobically (*Ef*, *Sm*, *Ss*, *Pa* and MRSA) at 37 °C according to the guideline. Except for *Pg* and *Fn*, which they were cultured in supplemented TSB, others were incubated in BHI broth medium. The bacteria at late log phase were diluted to the concentration with OD$_{660}$ value of 0.1 and performed for the following biological assays.

2.6. Antimicrobial activities of ellipsoids, rods and CBS

The minimum inhibitory concentrations (MICs) of the bismuth particles and CBS on the planktonic bacteria were determined by microdilution assay as described previously [20]. Generally, Ellipsoids, Rods and CBS were added to the 96-well plate filled with growth media, and a 2-fold serial dilution was performed with the highest treatment concentration of 1 mg/mL. Then, the bacteria (1.5×10^7 CFU/mL or 1.0×10^8 CFU/mL for MRSA) were transferred into the plate, making the final bacterial concentration 1×10^6 or 1×10^7 CFU/mL for MRSA, respectively. Upon obtaining the MIC values, 3 μL of each inhibitory concentration aliquot were spotted onto blood agar plates to determine the minimal bactericidal concentrations (MBCs). The plates were either anaerobically/aerobically incubated according to their optimal growing conditions.

2.7. Interactive profiles of Bi particles with the selected bacteria

Samples seeded at MIC were collected after discarding the spent media and suspended in saline before plating on the Thermonox plastic coverslips (15 mm diameter, Thermo Fisher). Then, the coverslips were submerged in 2.5% glutaraldehyde of a PBS solution for 1 h, and the liquid was fully aspirated and discarded, followed by step-washing with PBS and a series of EtOH solutions (30, 50, 70, 85, 95 and 100%). Finally, the samples were air-dried prior to coating with platinum, and their interactive profiles with bacteria were examined under SEM and FE-SEM.

2.8. Synergistic effects of bismuth particles and amoxicillin

The checkerboard assays were conducted to determine the fractional inhibitory concentrations (FICs) as described elsewhere with minor modifications [46,47]. In short, the AMX stock solution with 2X MIC was added to the first numerically labeled row followed by a 2-fold serial dilution across the 96-well plates. In a separated 96-well plate, the Bi particles solution with 2X MIC was placed at the alphabetically labeled column and then serially diluted across all wells. The two plates were subsequently mixed, making the final concentrations of both bismuth particles and amoxicillin at 1X MIC. Lastly, the bacterial cells were added to the wells, and the plate was incubated for 24 h.

2.9. Metal-releasing activities of the bismuth particles

Tissue culture plate inserts with polyester membrane (12 holes, 0.4 μm, JETbiofil, Guangzhou, China) were employed to evaluate the metal-releasing activities of the bismuth particles. Briefly, bismuth particles were first suspended in the upper or lower compartment of the plate. After the particles were evenly distributed in the media, *Pg* was added into the lower compartment and incubated for 72 h; afterward, the solutions were collected and the aliquots were spotted on a blood agar plate. Finally, the concentration of bismuth ions was analyzed through inductively coupled plasma optimal emission spectrometry (ICP-OES, Spectro Arcos, Kleve, Germany).

2.10. Anti-biofilm assays

Anti-adhesion and eradication experiments were performed on *Aa* and *Pg* based on MIC results and reported protocols with minor modifications [20,48]. Briefly, crystal violet (CV) staining, TTC colorimetric analysis and colony-forming units (CFU) enumeration were used for evaluating biofilm biomass, metabolic activities and bacterial cell viability, respectively. In the anti-adhesion assays, 10 μL of Bi particles/CBS solutions and 90 μL of bacteria were added to the 96-well plates. For the TTC colorimetric analysis, an additional 1 μL of 5% TTC solution was quickly added to the wells after giving treatments to bacteria, and the plates were immediately incubated under static anaerobic settings and grown accordingly to the predetermined optimal growth conditions of the selected bacteria (2 d for *Aa* and 3 d for *Pg*). After incubation, each well was washed with DI H_2O twice, followed by adding 105 μL of MeOH and incubating for another 30 min to allow dissolving of TTC-reduced formazan. The final metabolic activity was determined as:

Biofilm metabolism (%) = (Sample$_{A500}$ − Sample Blank$_{A500}$)/(Control$_{A500}$ − Blank$_{A500}$) × 100

For the CV staining, the plates with Bi particles/CBS and bacteria suspension were firstly incubated for 2 or 3 d. Then, the media were removed and the biofilms were subsequently washed with DI H_2O twice before quantifying the biofilm biomass with 0.1% of CV solution for 10 min. After that, the staining solution was discarded, and the CV-stained wells were washed with DI H_2O twice and incubated with 30% of acetic acid for another 10 min. The CV absorbance was recorded at 595 nm, and the following equation was applied for evaluating the effects of Bi particles/CBS on biofilm biomass:

Biofilm growth (%) = (Sample$_{A595}$ − Sample Blank$_{A595}$)/(Control$_{A595}$ − Blank$_{A595}$) × 100

Regarding CFU enumeration, the plates with treatments and bacteria were cultured for 2 or 3 d. Afterward, all liquid was aspirated from the plates, and each well was rinsed with fresh growth media two times to remove planktonic cells. The adhered biofilms were harvested by a cotton swab and transferred to an Eppendorf tube containing 1 mL of growth media. After vortexing for 5 min, the sample solutions were diluted, plated on the marked agar plate and incubated under optimal growth

conditions for at least three days. Then, the colonies were counted for determining bacterial viability.

Assays for biofilm eradication were similar to biofilm anti-adhesion. Generally, bacteria in their corresponding culture media were grown to late log phase and diluted to OD$_{660}$ of 0.1 before transferring 100 μL to the 96-well. After incubation, the planktonic and unadhered cells were removed by washing two times with PBS. Except for the TTC plate, which required adding another 2 μL of 5% TTC solution to each well (final concentration: 0.05% wt/vol), all plates were added with 20 μL of treatments (Bi particles or CBS) and 180 μL of fresh growth media, and further incubated with the biofilms for 24 h. The results of CV, TTC and CFU plates were collected and analyzed as described previously.

2.11. Confocal scanning laser microscopy

All anti-biofilm setups were identical to previous sections except that the bacteria were cultured in ibidi GmbH μ-Slide 8-well chambers with a polymer coverslip (Munich, Germany). After removing the treatments, the biofilms were stained with SYTO9 and propidium iodide from Live/Dead BacLight™ viability kit (Thermo Fisher Scientific) for 30 min at room temperature, and the biofilm viabilities were assessed using a confocal scanning laser microscope equipped with 543 nm HeNe laser and 488 nm Argon laser (Olympus FLUOVIEW FV 1000 with an FV-10 ASW system; Tokyo, Japan). The as-obtained fluorescence images were analyzed by ImageJ (Version 1.8.0, National Institutes of Health, USA).

2.12. Cell culture and cytotoxicity assays

Human gingival fibroblast cell line (HGF-1) was ordered from ATCC (Manassas, USA), while Dulbecco's modified eagle's medium (DMEM) and the fetal bovine serum (FBS) were ordered from Gibco (Thermo Fisher Scientific, Waltham, USA). HGF-1 was cultured in DMEM supplied with 10% FBS and 100 μg/mL of the antimicrobial agent Primocin (InvivoGen, USA) at 37 °C with 5% CO_2 in the humidified incubator. Then, HGF-1 was seeded in 96-well plate at the dentistry of 8×10^3 cells/well and cultured for two days to reach 80% confluency. Then, Bi particles and CBS at different concentrations (500, 250, 125 and 62.5 μg/mL) were added to the cells for 24 h, respectively. Then, the viability of the cells was assessed using Cell Counting Kit-8 (CCK-8, Dojindo, Kumamoto, Japan), and the permeability of the cell membrane was evaluated by CyQUANT LDH Cytotoxicity Assay Kit (Thermo Fisher Scientific, Waltham, USA).

2.13. Statistical analysis

All biological experiments were performed with at least two duplicates on three different occasions. The results were analyzed using GraphPad Prism 9 and presented as mean ± SD. The significant inter-group difference was analyzed using one-way analysis of variance with multi-comparisons by Bonferroni's test.

3. Results and discussion

3.1. Characterization of the two featured bismuth particles – Ellipsoids and Rods

Two different types of bismuth-based materials were synthesized with two commonly used precursors, trimesic acid (H_3BTC) and $Bi(NO_3)_3 \cdot 5H_2O$, *via* an ultrasound-assisted or agitation-free method (Scheme 1a). The morphologies of the as-synthesized bismuth materials were confirmed by FE-SEM and TEM with elemental mapping (Fig. 1b and S1), and the two as-identified micron-sized ellipsoid- and rod-like bismuth materials were denoted as Ellipsoids and Rods, respectively. Ellipsoids comprised of stacked thin-ellipsoidal sheets have an average measured length and width of 1.71 ± 0.35 and 0.40 ± 0.10 μm, respectively; whereas Rods with hexagonal facet have an average

measured length and width of 3.93 ± 0.42 and 1.92 ± 0.19 μm, respectively (Fig. S1). In this study, the H₃BTC ligands, a widely adopted and commercially available compound, were adopted as the linking agent. This bridging compound has been applied for synthesizing various types of MOFs, such as MIL-100(Fe), HKUST-1 and MOFs-808 [49–51]. It could act as a hard base by possessing carboxyl groups that bind to high-valent Bi^{3+} ions and form a stable structure [52]. Additionally, when DMF was selected as the solvent system, both ligand and metal starting reagents could completely homogenize in the solution, while only ligands could be dissolved in MeOH. Since the formation of crystal structures is solvent-dependent, MeOH as a solvent system may allow fast precipitation of the particles during the initial stage, whereas the usage of DMF may affect the solubility and interactions of the chemicals [53,54].

Utilizing an ultrasound device and adding a modulator, on the other hand, could facilitate and accelerate the formation of bismuth-based materials (Ellipsoids) in DMF. Of note, white precipitates of Ellipsoids could be fast observable within 10 min. Compared with previously reported hydrothermal/solvothermal methods, which usually take more than 10 h for each experiment, this approach may allow fast production due to increased pre-exponential factors [55]. Concurrently, adding modulators, such as NaOAc, could deprotonate the linkers and lead to fast nucleation, thus reducing the size of the particles to smaller scales.

Meanwhile, the powder X-ray diffraction (PXRD) patterns of Rods at low angles (below 10°) demonstrate similar peaks to CAU-17 stimulation, whereas the disappearance of several peaks of the poorly-crystalline Ellipsoids suggested a different form of bismuth material (Fig. 1c) [56].
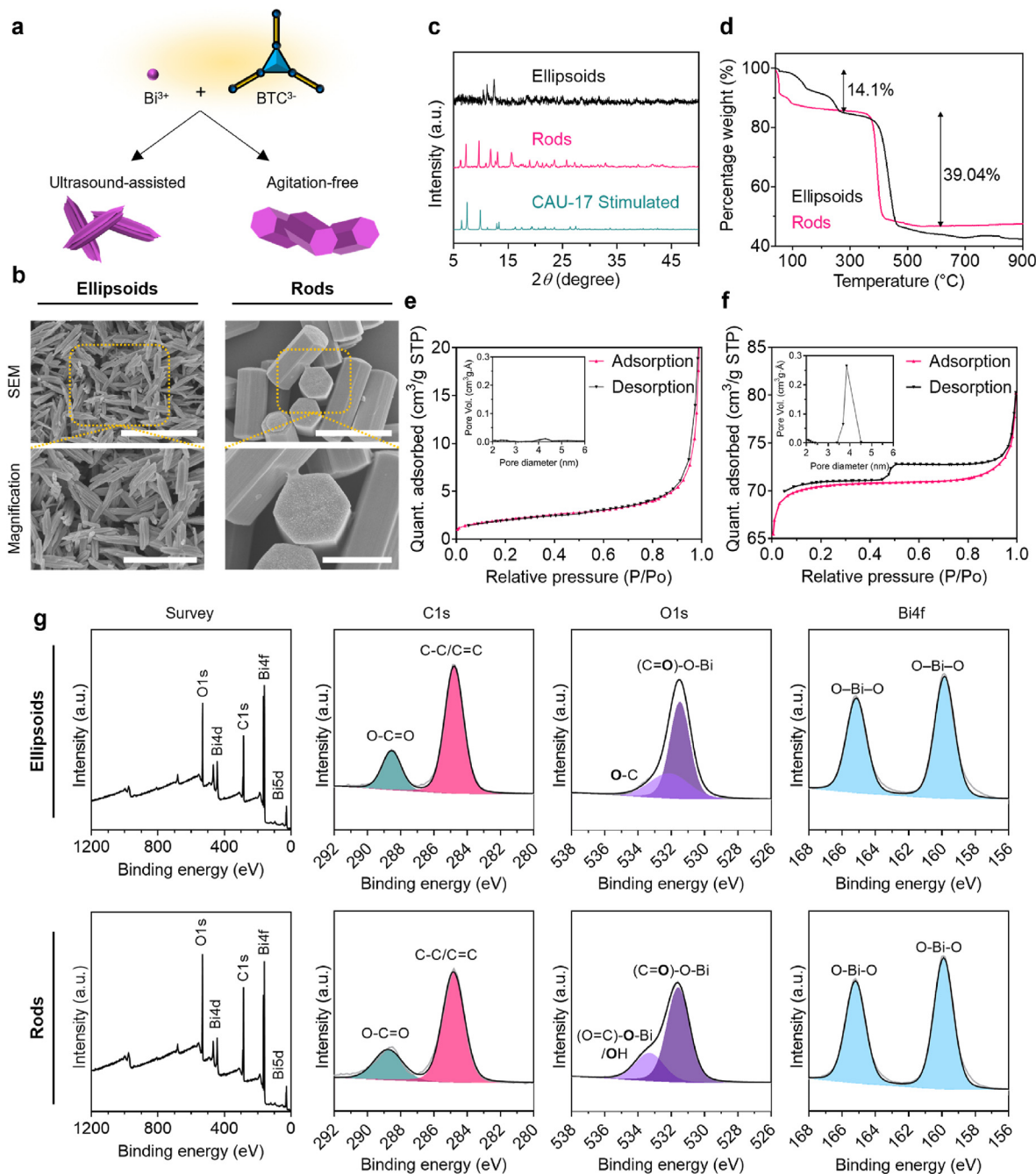

Fig. 1. (a) Schematic illustration of Ellipsoids and Rods syntheses. (b) Representative SEM images (scale bar: 5 μm) with magnification of Ellipsoids (scale bar: 3 μm) and Rods (scale bar: 2 μm). (c) PXRD patterns of Ellipsoids, Rods and CAU-17-stimulated. (d) TGA decomposition curves of Ellipsoids and Rods. N₂ adsorption-desorption isotherms of (e) Ellipsoids and (f) Rods with their BJH desorption dV/dlog(D) pore size distributions (insect). (g) XPS analysis of Ellipsoids and Rods.

According to Bennett et al., the poor crystallinity might be due to the presence of an amorphous phase resulting from the absence of long-range ordered structures in the crystal [57]. Additionally, the crystallinity patterns of Rods are highly consistent with the stimulated CAU-17, implying the formation of the CAU-17 MOF subtype, while the difference in peak intensity might be due to the disordered pore-blocking intermediates/precursors [56,58]. Furthermore, the Ellipsoids and Rods demonstrated similar thermal stabilities with each other according to the thermogravimetric analysis (TGA) (Fig. 1d). In general, both Ellipsoids and Rods shared a comparable weight loss pattern, except that Ellipsoids had an extra mass loss to 160 °C. The first two mass losses to 110 °C and 160 °C indicate the removals of solvents [59]. Consequently, the last mass loss to 400 °C suggests the decomposition of the H$_3$BTC.

The Brunauer-Emmett-Teller (BET) analysis further determined the porosity of the as-synthesized particles. It was found that Ellipsoids (Fig. 1e) had a surface area of 7.46 m^2/g, while Rods had a BET surface area of 228.77 m^2/g with an average adsorption pore width of 2.02 nm. Moreover, the N$_2$ adsorption-desorption isotherms of Rods could be classified as a typical type IV isotherm accompanying H3 hysteresis with a relative pressure (P/P_o) between 0.5 and 0.9 (Fig. 1f), which were commonly recognized in MOFs [53,60,61]. These data indicate the non-porous structure of Ellipsoids and support that Rods with MOF nature contain porous architecture. It was also noted that the surface area of Rods was less than that of the reported CAU-17 synthesized via the hydrothermal approaches (228.77 vs. 530 m^2/g) [44], which might be owing to the incomplete activation of Rods prior to the N$_2$ adsorption/desorption analysis.

Fourier transform infrared spectroscopy (FT-IR) and X-ray photoelectron spectroscopy (XPS) were undertaken to determine the functional groups and bindings as well as the elemental composition of the particles. As presented in Fig. S2, Ellipsoids and Rods showed almost identical FT-IR spectra, which could also be found in the previous report [62], while the three peaks of the H$_3$BTC spectrum at 3200–2700 cm^{-1}, 1730–1706 cm^{-1} and 1440–1395 cm^{-1} disappeared after crystallization, demonstrating the opening of the metal site centers to form bismuth materials. Moreover, XPS analyses were conducted to understand the detailed elemental compositions of Ellipsoids and Rods. As revealed in Fig. 1g,

both bismuth particles primarily consisting of C, O and Bi had nearly identical elemental composition profiles. Generally, the C1s of the two particles could be divided into two bands, the C–C/C=C at 284.8 eV and O–C=O at 288.6 eV. Meanwhile, the O1s bands could be identified as the bindings of (C=O)–O–Bi at 531.5 eV and **O**–C at 532.1 eV or the bismuth-oxo clusters (O=C)–**O**–Bi/**O**H at 533.3 eV. For the Bi4f spectra, the doublet peaks at 159.8 and 165.2 eV could be ascribed to the O–Bi–O binding [63,64]. Taken together, we speculated that the variation in crystallization and morphology might not be due to their elemental compositions but the arrangement of their initial building blocks resulting from different synthetic approaches.

3.2. Effects of various synthetic conditions on the crystallization of rods

The hexagonal rod-like MOFs (Rods) could self-assemble under ambient conditions via a stirring-free direct precipitation method. We hypothesized that their formation might be associated with the orientation of the initial building blocks (Fig. 2a). Therefore, a time-resolved study was carried out to investigate the effects of agitation (stirring) on the crystallization process. An aliquot of each experimental group was collected every 5 min for a total of 30 min, and its morphology was determined under SEM. As shown in Fig. 2b, a re-arrangement would occur for the first 5–10 min before transforming the "oblongs" to the as-seen structures. Briefly, the Rods underwent two observable phase transitions in the solution prior to their precipitation. The first transition (cloudy to transparent in MeOH) happened within the first 1–2 min after the starting materials were completely sonochemically dissolved. The second transition took place in the next 20 min with aggregates of the white precipitates gradually becoming apparent in the reagent bottle. Interestingly, if stirrings were employed at any time, the Almond-flakes would appear, whereas the Rods would only form when no agitation was applied.

To further support our hypothesis, a parallel setup with the assistance of an ultrasound device was performed to investigate the effects of disturbance on the formation process of MOF, and the as-synthesized particles were denoted as Ultrasound. As shown in Fig. S3a, bismuth particles synthesized with stirring (denoted as Agitation) or the
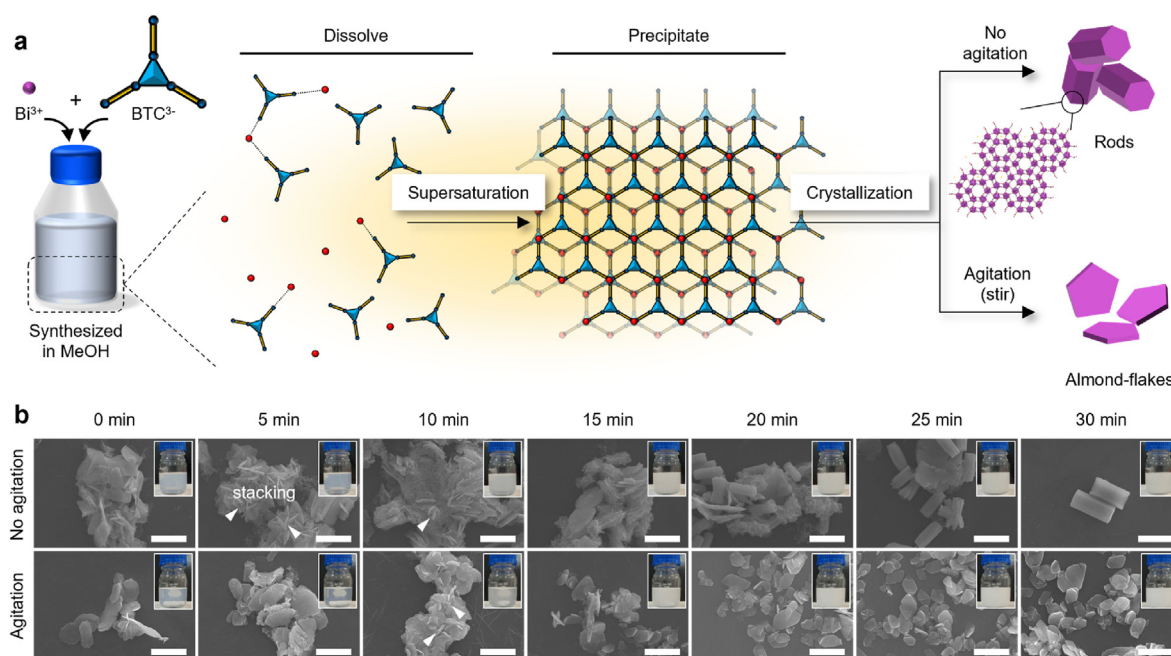

Fig. 2. (a) General scheme of crystallization course of Rods. The turbidity of the reaction solution and (b) the SEM images of the precipitations at each time point from the reactions with or without agitation. An aliquot was taken out from the solution every 5 min for 30 min. If stirrings were employed, Almond-flakes would appear, whereas the Rods would only form when no agitation was applied (scale bar: 5 μm). White arrowheads indicate the stacking of the "oblong" building blocks. Depending on the synthetic methods, these building blocks aligned differently could affect their orientation during the synthesis, resulting in different structures.

assistance of an ultrasound device could form Almond-flake-like shapes, and their physicochemical properties such as elemental compositions and crystallinity assessed by XPS and XRD were almost identical. The XPS spectra of all bismuth particles in Fig. S3b did not reveal significant shifts in their chemical bindings, except for O1s. Remarkably, the employment of an ultrasound device may lead to an increase in the formation of C–O bindings. Meanwhile, the elemental compositions of the bismuth materials (Fig. S3c) demonstrated that Ellipsoids, ultrasound-assisted and agitated Almond-flakes had similar atom composition profiles, whereas Rods had the least amount of bismuth percentage. Referring to the XRD patterns of the bismuth particles (Fig. S3d), the agitated Almond-flakes displayed almost identical peaks to the sonochemically prepared ones, which was similar to the "plates" found in previous studies [53,56,65, 66]. These flakes/plates in the absence of distinct peaks at a low angle ($2\theta < 10°$) have been considered as the intermediates of CAU-17 generated from the initial nucleation points, and they may have a close association with the homogeneity and axial-growing of the sonochemically synthesized CAU-17 [56], Taken together, the utilization of different synthetic approaches as well as the selected solvent systems may have minimal effects on the elemental compositions of the particles. Yet, it may greatly affect the orientations of the intermediates during the early crystallization phase.

To the best of our knowledge, all currently reported Bi-MOFs were prepared through either hydrothermal, solvothermal, mechanochemical or sonochemical methods, which usually required high temperature and pressure, long reaction time and additional supporting devices. These Bi-MOFs were mainly designed for non-biological purposes, and their synthetic conditions and applications are summarized in Table S1. Of note, we are the first group to report the rapid and facile approach to synthesizing Bi-MOFs in MeOH at room temperature. Under the same scale of synthesizing CAU-17, the final mass produced from the method used in this study was 48.4 mg (equivalent to 68.5% of metal conversion), whereas the final mass prepared with the most frequently reported hydrothermal methods (120 °C for 24 h) was 38.6 mg (metal conversion: 54.6%) (Fig. S4). Meanwhile, the Rods constructed in this study were better defined, more uniform structure yet with less debris than those obtained from the hydrothermal reaction. It is worth noting that our repeating experiment using the previously reported hydrothermal method for synthesizing CAU-17 did not generate equivalent rod-shaped crystals, suggesting that the anticipated high repeatability could not be obtained through the widely adopted approach. Lastly, the rod-shaped MOFs with scale-up yield could be quickly harvested within 30 min by increasing the reaction volume to 240 mL (8 folds of the original reaction set), indicating a highly repeatable synthesis and stable process of crystal formation.

Besides the high metal conversion, the aforementioned results clearly indicated that at least two key stages were involved in the crystallization of Bi-MOF, *i.e.*, the formation of the Almond-flake-like units and their subsequent stacking into the rod-like structure. It has been suggested that the crystallization of MOFs is determined by nucleation and growth [67, 68]. According to classic nucleation theory, the crystalline nuclei generated from the starting materials under supersaturation conditions favor a more thermodynamically stable phase, leading to an irreversible shift of their shapes [68]. In this study, the H_3BTC ligand exhibits good solubility in MeOH, while the Bi source is insoluble in alcohol. Interestingly, when these two chemicals were simultaneously applied to MeOH, they could temporarily dissolve under sonication. This short-term dissolved status might be due to the high-affinity binding between the carboxyl groups of H_3BTC and Bi ions. When the dissolved Bi ions became supersaturated, the crystallization commenced alongside the gradual appearance of white precipitates in the solution, suggesting the formation of Almond-flake-like units and their self-assembly of rod-like structures (Fig. 2a). Therefore, in addition to the effects of agitation, the initial metal concentrations ([M]) and the metal-to-ligand (M-L) ratios may play a critical role in the precipitation rate, which may consequently influence the size of the Almond-flake-like units and the

following self-assembled rod-like MOF shapes.

As shown in Fig. 3a, when the values of [M] were at 1 mM and 5 mM, the oblong-like flakes were firmly stacked until the M-L ratio exceeded 1:10 and 1:1, respectively. Thereafter, the flakes were replaced by thinner and more elongated rod-like structures. For [M] at 10 mM and 20 mM, only an insignificant number of oblong-flake fractures could be identified with 1:1 and 1:5 M-L ratios, while most of the shapes were smaller and thinner rods. Moreover, the duration of the as-observed transparent phase was obviously prolonged, while the M-L ratio increased. As presented in Fig. 3b, the length, width or aspect ratio vs. [M] of Rods with various M-L ratios was calculated, respectively. Notably, the width of the Rods significantly decreased to nano-scales with [M] at 10 mM and 20 mM as well as M-L ratios of 1:20 and 1:30. These findings reveal that the formation of Rods highly relies on Bi ions reaching the supersaturation point under proper M-L ratios in the first place. Importantly, increasing the amount of ligands could facilitate the depletion of the local metal ions and lead to the formation of smaller crystal units, particularly at higher metal concentrations, thereby enabling tunable synthesis of CAU-17 from micro-to nano-scale.

3.3. Stability of Ellipsoids and Rods in various solutions and media

The stability of Ellipsoids and Rods in various solutions and media, such as DI H_2O, PBS, TSB and BHI, was also investigated (Fig. 4 & S5). In general, both Ellipsoids and Rods could maintain their overall morphology with no or minor degradation when immersed in DI H_2O or the growth media for up to 14 days. It has been previously reported that MOF instability in DI H_2O possesses an initial concentration-dependent manner, depending on the hydration-deprotonation equilibrium. Meanwhile, the small amount of degradation in bacterial media might be due to the metal ion binding with the organic species and subsequently forming water-soluble organometallic moieties [69]. However, when PBS was selected as the solution system, the skeleton of the particles started to collapse after the 4th day, resulting in a thread-like morphology with tiny bubbles attaching to the edges. On the 14th day, both bismuth particles completely lost their integrity (Fig. S5). According to Orellana-Tarva et al., these tiny bubbles adhering to the surface could lead to the decomposition of the particles [70]. Similar results are found in the previous studies of UiO-66 Zr-based MOFs, in which the phosphate in PBS may replace the linkers, resulting in particle degradation [69–71]. In sum, both Ellipsoids and Rods demonstrated excellent stability in DI H_2O, TSB and BHI. The stability of bismuth particles in these media may be further employed for biological experiments, including antimicrobial and anti-biofilm assays.

3.4. Cytotoxicity tests of Ellipsoids and Rods in human gingival fibroblast cell line (HGF-1)

The potential effects of Ellipsoids, Rods and CBS on the viability of HGF-1 were evaluated *via* the CCK-8 and LDH assays. No detectable toxicity was observed for CBS, in line with our recent findings.[9] Of note, both Ellipsoids and Rods did not exhibit significant effects on the cell viability of HGF-1 (Fig. 5).

3.5. Antimicrobial effects and interactive profiles of Bi-based materials against selected bacteria

The antimicrobial effects of the Bi particles on the eight representative bacteria in both planktonic and biofilm modes were assessed. Overall, Ellipsoids and Rods exhibited similar results to CBS (Table 1). All bismuth treatments were more effective against Gram-negative than Gram-positive bacteria. Specifically, Ellipsoids had a MIC value of 1000 μg/mL, whereas both Rods and the CBS control groups had MIC values of 125 μg/mL for *Sm*. As for *Ss*, Rods and Ellipsoids exhibited minimum inhibitory effects at 500 and 1000 μg/mL, respectively; while CBS did not demonstrate any bacterial inhibition. It was noteworthy that Ellipsoids,
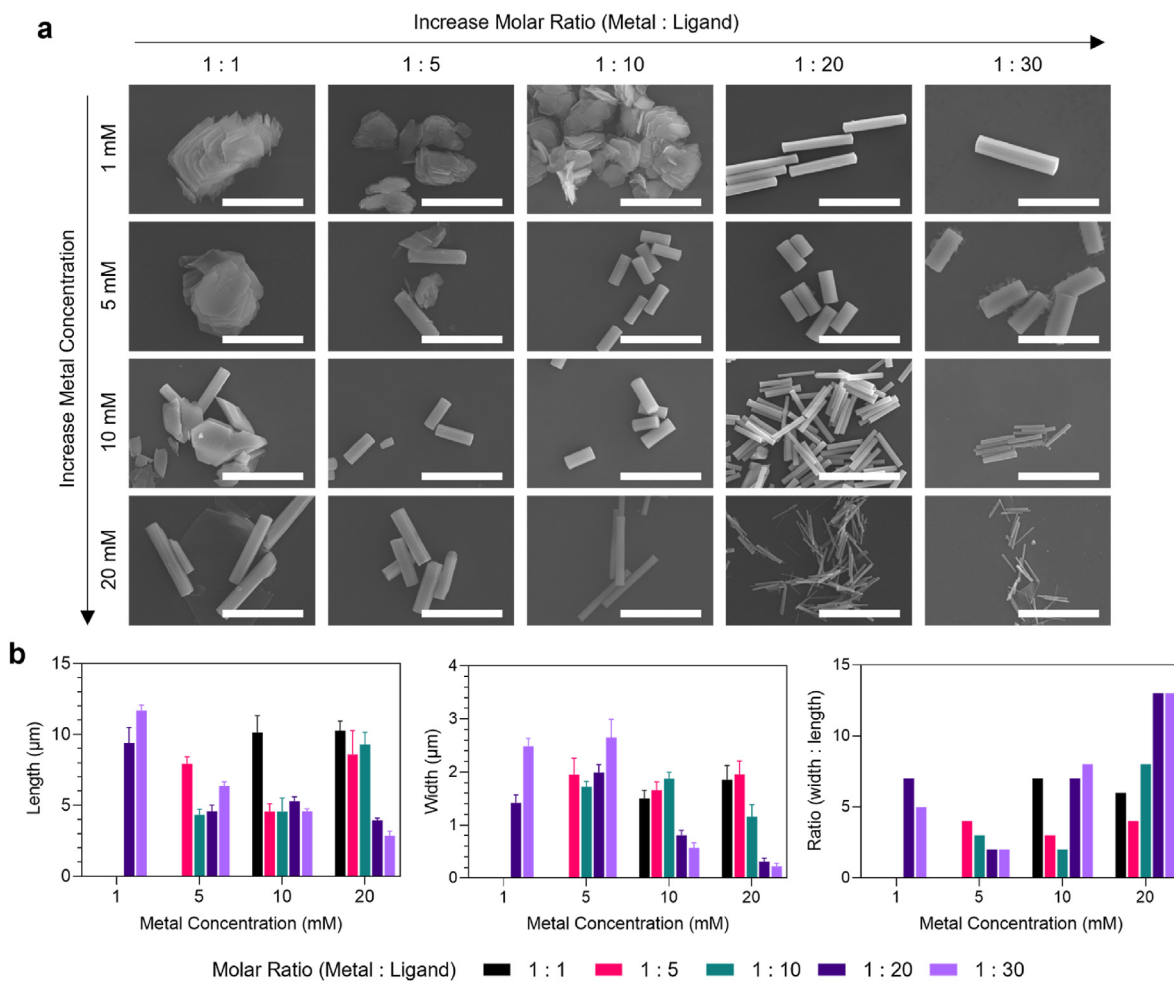
Fig. 3. (a) Effects of initial metal concentrations ([M]) and metal-to-ligand (M–L) ratios by using a size-controlled synthesis of Rods. The "oblong-like" sheets were firmly stacked at lower M-L ratios and became the as-seen elongated rod-like structure with higher initial [M] (scale bar: 10 μm). (b) The combined bar charts of calculated length, width and aspect ratios vs. different [M] of the Rods synthesized from various M-L ratios.
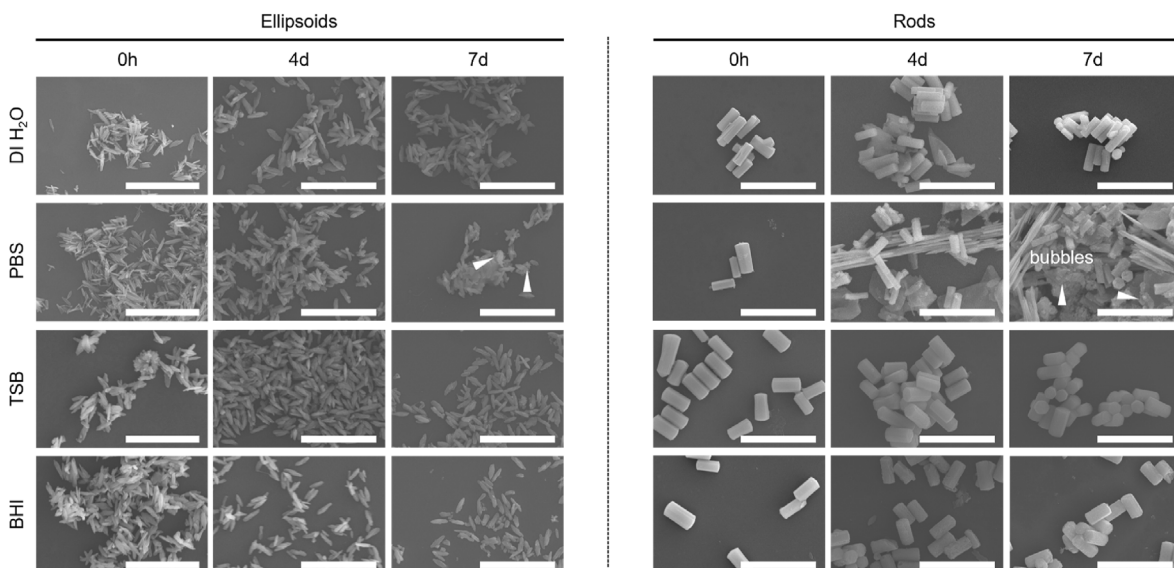

Fig. 4. Material stability of Ellipsoids and Rods in different solutions and culture media (DI H$_2$O, PBS, TSB and BHI) for up to 7 days (scale bar: 10 μm). Both bismuth materials could maintain their integrity in the abovementioned solutions/media except in PBS. The white arrowheads indicate the formation of bubbles adhering to the surface of the particles.
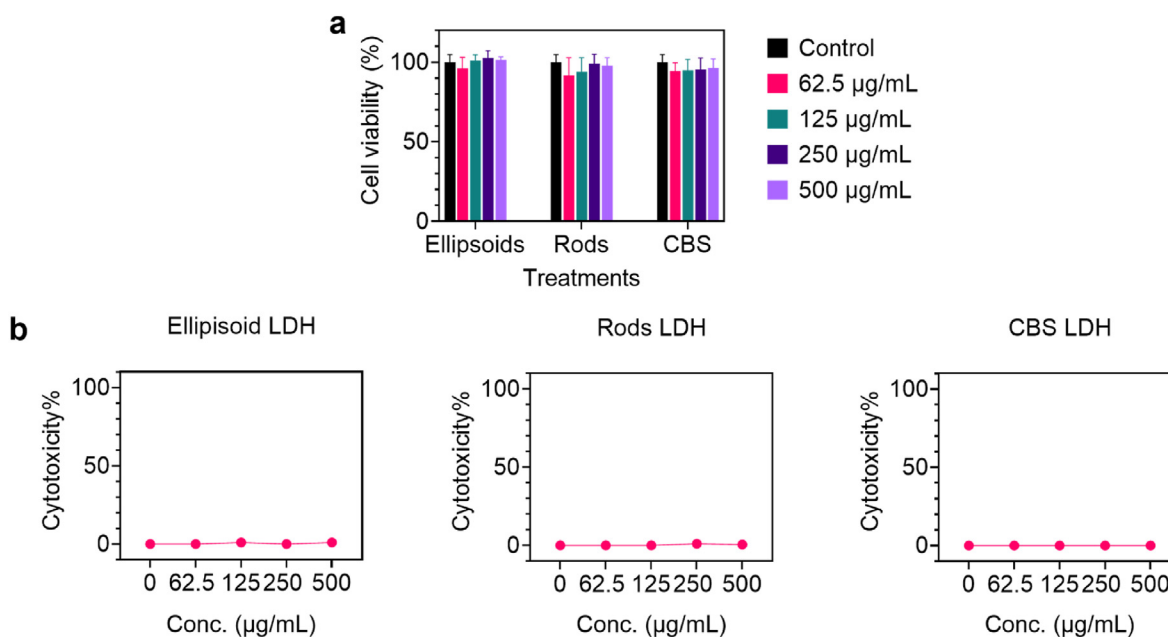
Fig. 5. CCK-8 and LDH assays for evaluating (a) the cell viability of Ellipsoids, Rods and CBS and their (b) cytotoxicity in human gingival fibroblast cell line (HGF-1), respectively. The histograms and line are presented as mean ± SD. For the cytotoxicity of the bismuth-based particles in HGF-1, both Ellipsoids and Rods together with CBS did not exhibit detectable toxicity.

Table 1
Minimum inhibitory concentrations (MICs; µg/mL) and minimum bactericidal concentrations (MBCs; µg/mL) of Ellipsoids, Rods and CBS against the eight bacteria tested.

Species	Ellipsoid	Rod	CBS
Minimum inhibitory concentrations (MICs; µg/mL)			
Gram (+) bacteria			
E. faecalis	>1000	>1000	>1000
MRSA	>1000	>1000	>1000
S. mutans	1000	125	125
S. sorbrinus	1000	500	>1000
Gram (−) bacteria			
A. actinomycetemcomitans	7.8–31.3	7.8–31.3	31.3
F. nucleatum	<2.0	<2.0	<2.0
P. gingivalis	7.8	7.8	7.8
P. aeruginosa	>1000	>1000	>1000
Minimum bactericidal concentrations (MBCs; µg/mL)			
Gram (+) bacteria			
E. faecalis	>1000	>1000	>1000
MRSA	>1000	>1000	>1000
S. mutans	>1000	>1000	>1000
S. sorbrinus	>1000	>1000	>1000
Gram (−) bacteria			
A. actinomycetemcomitans	31.3	31.3	31.3
F. nucleatum	7.8	3.9	3.9
P. gingivalis	62.5	31.3–62.5	31.3
P. aeruginosa	>1000	>1000	>1000

Rods and CBS exhibited promising antimicrobial properties against planktonic Gram-negative bacteria *Aa*, *Pg* and *Fn* except *Pa*. In a related manner, Rods synthesized with different [M] and M-L ratios showed no differences in their antimicrobial activities on the three periodontopathogens tested (Table S2), suggesting that all types of Rods shared the same crystalline structure of CAU-17 regardless of the number of Bi ions doped into the MOF skeleton. The Rods synthesized with [M] at 5 mM and M-L of 1:10 were therefore selected to represent all sizes of CAU-17 MOFs for the subsequent bactericidal assays, on the basis of their high Bi% conversion and the same metal concentration/M-L ratio used by the Ellipsoids. Their MBCs were subsequently spotted on blood agar plate upon MIC determination, and the results were tabulated and presented in Table 1 & Fig. 6a. The MBC findings demonstrate similar MIC results.

Notably, the three periodontopathogens (*Aa, Fn* and *Pg*) [72] completely lost viability at 31.3 µg/mL. Representative Gram-staining optical microscopy and SEM images (Fig. 6b) further showed the effects of bismuth treatments on *Aa*, *Fn* and *Pg*. Some bacterial cells treated by the as-synthesized particles underwent subtle morphological changes. Importantly, the fragmented bacterial cells attached to the Rods could not maintain their structural integrity.

Collectively, Ellipsoids, Rods and CBS demonstrated potent antimicrobial/bactericidal effects, particularly on Gram-negative periodontopathogens. These bacteria could consume Bi^{3+} and subsequently facilitate the degradation of particles. Although the antimicrobial activities of the metallic particles were heavily dependent on the type of doped metals, the peptidoglycan-composed outer layer of Gram-positive bacteria could impede the crossing of the metal ions (*e.g.*, lead, silver and copper), leading to the resistance to the metals [73]. Therefore, amoxicillin (AMX), a broad-spectrum β-lactam antibiotic for inhibiting the biosynthesis of the peptidoglycan-composed bacterial cell walls [74], was selected to perform a combined treatment with the bismuth particles against *Ss, Sm, Ef* and MRSA using the checkerboard assay. As demonstrated in Fig. 7a and b, the fractional inhibitory concentration (FIC) indices with values from 0.5 to 1.0 indicated an addictive effect on suppressing *Ss, Sm* and MRSA, suggesting that the bismuth ions may affect the Gram-positive bacteria following the AMX treatment. Nevertheless, this finding was more apparent in *Ss* and *Sm*, implying that the antimicrobial sensitivity could be species-dependent, and more complicated mechanisms might be involved in the bismuth particles-antibiotic combined treatment.

Furthermore, bismuth ions released from the particles might be able to transport through the cell membrane, leading to the destruction of Gram-negative bacterial cells [73,75,76]. Surprisingly, despite promising results were found in the abovementioned bacteria, bismuth treatments did not exhibit potent antimicrobial effects against *Pa* even at the planktonic mode. Yet, it was observed that this cystic fibrosis-causing *Pa* secreted less viscous polysaccharide slime than the growth control group after the treatment with Bi-based particles for 1 d, corresponding to previous bismuth dimercaprol (BisBAL) findings [77]. The potential addictive effects of Bi particles and antibiotics (penicillin, PEN) could be observed in the checkerboard assay. It is worth mentioning that bismuth
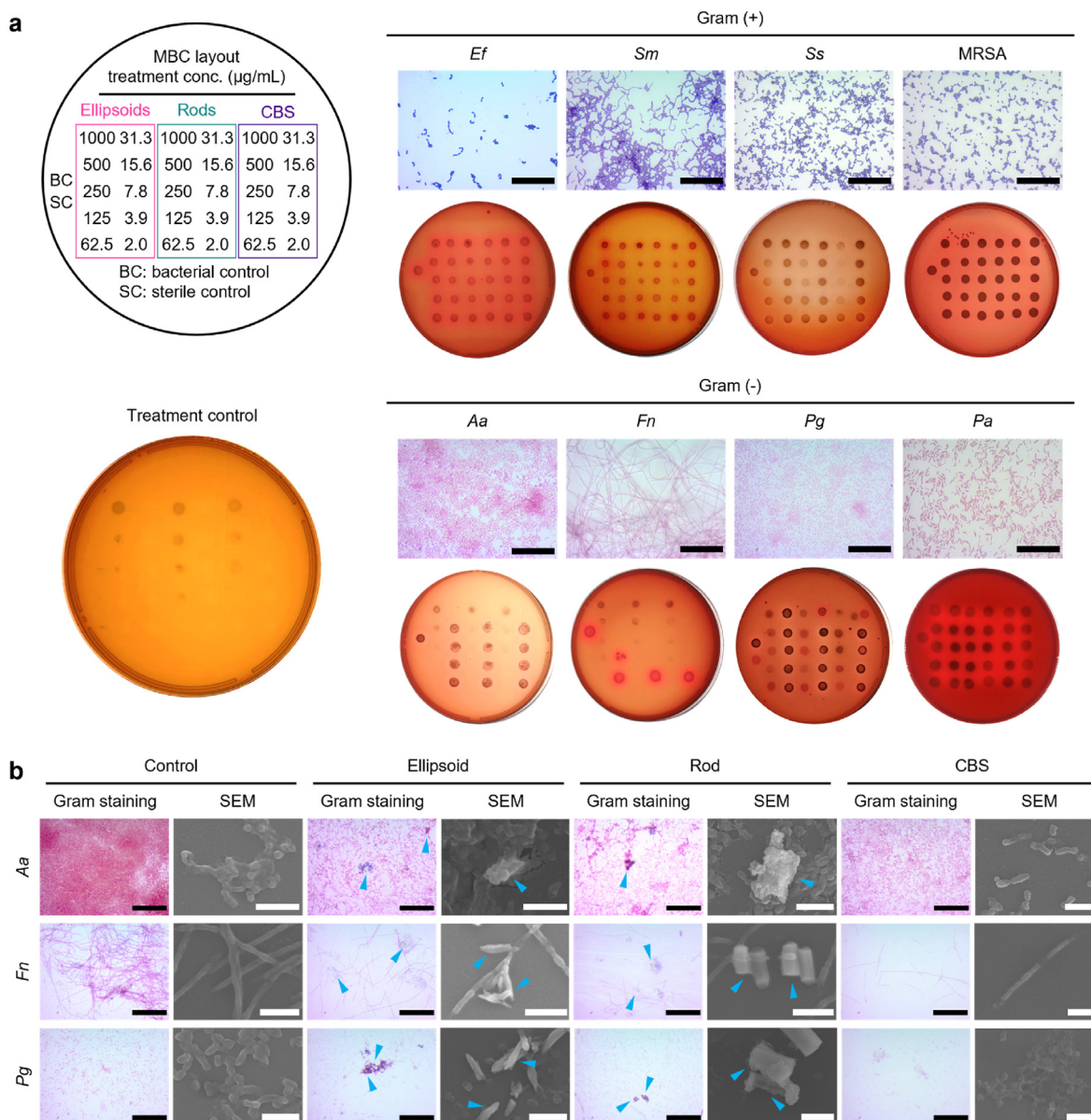
Fig. 6. (a) General MBC layout with different treatment concentrations (μg/mL) and treatment control group with representative images of Gram-staining microscope (scale bar: 20 μm) and MBC agar plates. (b) Representative Gram-staining optical microscopy (scale bar: 20 μm) and SEM (scale bar: 2 μm) images showing the interaction profiles of Ellipsoids, Rods and CBS against *Aa, Fn* and *Pg* with blue arrowheads indicating the particles. (For interpretation of the references to colour in this figure legend, the reader is referred to the Web version of this article.)

as an adjuvant may to some extent restore the activities of PEN (Fig. S6). Similar observations could also be found in the Gram-negative bacteria *Klebsiella pneumoniae*. According to Domenico et al., the capsular polysaccharide (CPS) of *K. pneumoniae* could provide a shielding effect and protect the bacteria from the host defense system. The bismuth compounds could inhibit the CPS expression and simultaneously enhance its potential to promote phagocytosis and antibody reactivity of lipopolysaccharide [78].

Apart from *Pa*, Bi particles showed similar inhibitory effects on both *Aa* and *Pg*, while *Fn* had significantly lower MIC values than other selected strains and exhibited higher sensitivity towards Ellipsoids, Rods and CBS compared to other bismuth materials such as bismuth subsalicylate nanoparticles (BSS-nano; 60% inhibition at 15.4–21.7 μg/mL) [79]. A 12-well plate with inserts was employed to investigate whether the bismuth ions released from the as-constructed particles participate in the bacteria-killing process. As illustrated in Fig. 8a, the bismuth particles (1 mg/mL) were first added either to the upper (filtered) or lower (not

filtered) compartment of the tissue culture insert with 0.4 μm pore size, followed by the addition of *Pg* in the lower compartment and incubation for 72 h. The clear aliquoted spots on the blood agar plate demonstrated that the treatments in all filtered groups could effectively inhibit the growth of *Pg* (Fig. 8b). Meanwhile, inductively coupled plasma optimal emission spectrometry (ICP-OES) also confirmed that the solutions collected from the lower compartment of the filtered groups ($E_{Filtered}$ & $R_{Filtered}$) contained a comparable amount of bismuth to the not-filtered groups, suggesting the release of bismuth ions from the frameworks of particles (Fig. 8c).

The antimicrobial potency towards these pathogens might be firstly associated with the disruption of bacterial defense system-generated compound hydrogen sulfide (H_2S) and metabolism. Notably, it has been confirmed that bismuth ions perturb the tricarboxylic acid (TCA) cycle and urease activity, thereby leading to oxidative stress that accounts for the suppression of *H. pylori* [80]. Meanwhile, early studies have reported that the volatile sulfur small molecule could play a pivotal
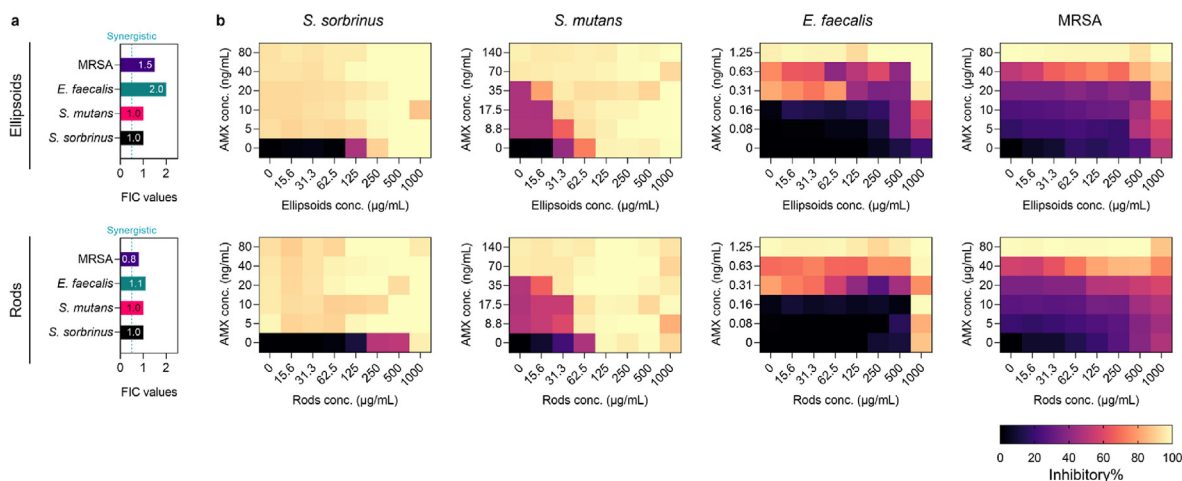
Fig. 7. (a) FIC indices and (b) the checkerboard analysis of the combined effects of amoxicillin (AMX) with Ellipsoids and Rods on *S. sorbrinus*, *S. mutans*, *E. faecalis* and MRSA.
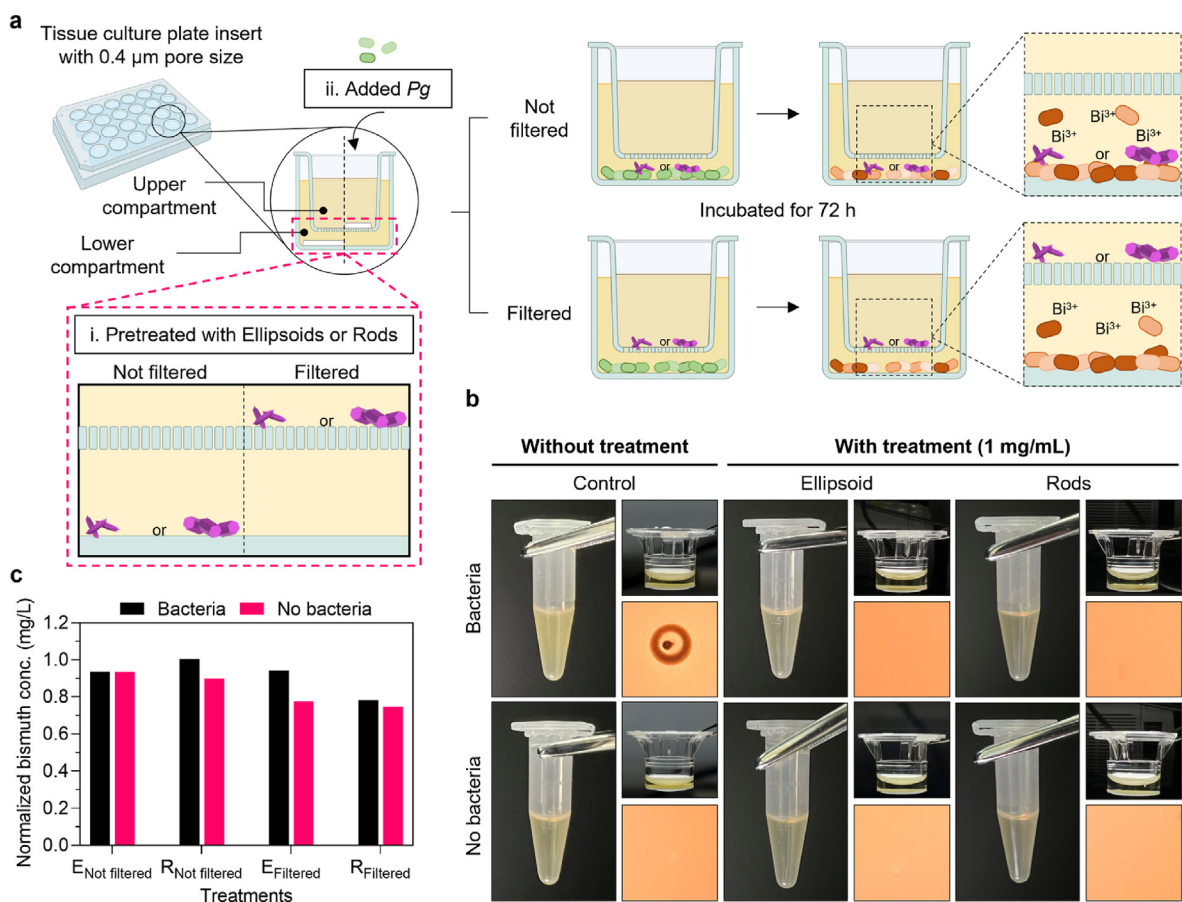

Fig. 8. (a) Illustrated scheme of investigating whether the bismuth ions released from the constructed particles participate in the bacteria-killing process using a 12-well plate with inserts. The solutions from the lower compartment were collected for (b) spotting on a blood agar plate and (c) ICP-OES analysis of the bismuth ions released from the particles.

role in the progression of oral diseases like periodontitis [81,82]. Indeed, *Pg* and *Fn* are the two heavy H_2S producers in human oral cavity [81]. Moreover, it has been considered that H_2S is the key molecule involved in the bacteria persistence and resistance to antibiotics; and conceivably, inhibiting H_2S biogenesis could sensitize bacteria to antimicrobial treatments [83–85]. In the present study, it could be speculated that the Bi^{3+} released from the Bi particles may contribute to the clearance of the

bacteria-generated H_2S *via* the redox reaction. Additionally, bismuth, having a high affinity towards S-, N- and O-containing functional groups (*e.g.*, cysteine, histidine, aspartic acid and tyrosine) of proteins or peptides in the biological systems [21,23], may disturb the iron-protein binding and consequentially perturb its multiple metabolic pathways, leading to ferric deprivation [16]. It is noteworthy that the metal ion could inhibit iron-associated bacterial proteins, such as gingipains and

hemagglutinin HagA of *Pg*, and subsequently affect the iron metabolic activities [20,23]. However, additional proteomic investigations are needed to further understand the underlying mechanisms of bismuth-driven bactericidal effects.

3.6. Effects of Ellipsoids and Rods on the mono-species biofilms of Aa and Pg

Biofilms, a unique microbial community that enormously grants survival advantages to its inhabitants, crucially account for the onset and development of various persistent infections and inflammatory diseases in dysbiotic conditions [86–89]. Given the potent anti-microbial/bactericidal activities exhibited in *Aa* and *Pg*, the two strains were further selected for anti-biofilm analysis. Their optimal biofilm growth conditions (mono-species *Aa* 2-day-old and *Pg* 3-day-old biofilms) were established simultaneously in the preliminary study and used for the subsequent biofilm assays. Here, *Fn*, one of the opportunistic pathogens residing in the human oral cavity having close association with colorectal cancer, was not chosen for the anti-biofilm assay due to low biofilm-forming activity and its biofilm model is best built with other oral bacteria in the multi-species model [90,91]. Further extended studies are therefore needed to perform the anti-biofilm assays in multi-species models.

As illustrated in Fig. 9a, the anti-adhesion and eradication effects of the materials on the biofilms were examined. Briefly, in the anti-adhesion experiments, Ellipsoids, Rods and CBS (500, 100, 50 and 10 μg/mL) were incubated with the bacteria of interest at a density of 1.5×10^7 CFU/mL for 2 (*Aa*) or 3 d (*Pg*). For eradication assays, the biofilms were grown to a mature state (2 d for *Aa* and 3 d for *Pg*) before adding treatment groups on the following day. After incubation for another 24 h, the biofilms were tested with confocal microscopy imaging, crystal violet (CV) staining, TTC tetrazolium salts colorimetry and colony-forming unit (CFU) enumeration for evaluating the viability, biomass, metabolic activities and bacterial cell viability, respectively [92].

Figs. S7 and 9b-e present the anti-biofilm results of *Aa* and *Pg*, respectively. The confocal laser microscopy was first performed to investigate the viability of the bismuth-treated biofilms in the anti-adhesion and eradication experiments. The number of SYTO9-labeled green fluorescent *Aa* cells declined significantly after the treatment with all bismuth particles (at least 50 μg/mL) as compared to the growth control group (Fig. S7a). A decreasing pattern of green fluorescent pixels could be found as the treatment concentrations increased (Fig. S8). Meanwhile, the same patterns could also be observed for the biofilm eradication (Fig. S7b) with visible red fluorescence highlighting the PI-labeled dead bacterial cells. Generally, as the treatment concentrations increased, the green fluorescent bacterial cells became sparser with increasing vivid red fluorescent bacterial cells.

Quantitative analyses further confirmed our observations. The CV staining and TTC colorimetry of the *Aa* anti-adhesion study indicated that the biomass and metabolic activities of all bismuth-treated biofilms had a significant decrease ($p < 0.05$) of the absorbance values at 595 and 500 nm, respectively (Fig. S7c). The subsequent CFU enumeration showed that the number of viable cells of the 2-day-old *Aa* biofilms at the anti-adhesion assessment decreased by at least 100 times for all treatment groups with reference to the control group at 500 μg/mL with a significant difference for Ellipsoids ($p < 0.05$) and CBS ($p < 0.01$), respectively. Surprisingly, all treatments exhibited relatively weak anti-biofilm activities for eradication of *Aa* biofilms (Fig. S7d). Although CV and TTC measurements also showed a less dramatic decreasing trend of biomass and metabolic activities as the concentration increased, the number of countable colonies from the CFU values did not reveal any significant differences.

The inhibition potency towards the growing biofilms of *Aa* suggests that bismuth might interfere with the formation of *Aa* biofilms at the early stage, thereby significantly reducing the number of adhered bacterial cells. However, when mature *Aa* biofilms were presented, the

potency of bismuth ions was compromised, possibly due to the Bi^{3+} binding to the negatively charged extracellular polysaccharides from the biofilm matrix that greatly hindered the diffusion efficiency of the particles. This result suggests that bismuth treatments against *Aa* could effectively eliminate the planktonic bacterial cells at the early stage of biofilm attachment. Yet, complete eradication of the *Aa* mature biofilms might require additional approaches, such as the addition of an antibiotic or modification of penetrating peptides/polymers, to facilitate the entering of bismuth into the interior of biofilms.

Referring to the anti-biofilm assays of *Pg*, the confocal images revealed that the treatment of Bi particles demonstrated similar inhibitory effects on its early biofilm formation (anti-adhesion) as well as the mature ones (eradication), and these inhibitory effects were dramatically enhanced along with the increased particle concentrations (Fig. 9b and c and S9). Meanwhile, the presence of both Ellipsoids and Rods could be observed at the treatment concentrations of both 500 and 100 μg/mL in the biofilm eradication model (Fig. S10a). The fluorescence-highlighted Rods, compared with Ellipsoids, displayed more vivid and filled green pixels on the surface of the particles, which could be due to the encapsulation of SYTO9 in the porous structures.

For the assays against *Pg* biofilms, all the bismuth treatments with concentrations over 10 μg/mL were able to decrease the number of bacterial cells as compared to the control group, displaying fewer green fluorescent dots overall. Likewise, the 10 μg/mL-treated *Pg* biofilms revealed a slight morphological change by transforming some bacterial cells from a round into an oval shape (Fig. S10b), suggesting the alternation of the cellular morphology and structures [20]. It is also noteworthy that the intensity of the red fluorescent PI was significantly lower in the biofilm models of *Pg* compared to that of *Aa*, and similar findings could be reflected in other reports [93,94]. Since the survival mechanism of *Pg* is heavily dependent on its iron-acquiring ability [95], bismuth as iron-binding inhibitors for multiple proteins may compete with iron and simultaneously induce oxidative stress *via* generating free radicals [20]. These radicals may further damage the bacterial DNA and prevent the binding of nucleic acid-staining dyes, SYTO9 and PI, thereby resulting in weak fluorescent signals under confocal [96].

On the other hand, CV and TTC values revealed a more dramatic decrease in both inhibition (Fig. 9d) and eradication (Fig. 9e) models of *Pg* biofilms than *Aa* biofilms. Moreover, all treatment groups at various concentrations showed significant differences ($p < 0.05$). In particular, black sediments were found in the bismuth-treated *Pg* samples, and no or little black sediment could be detected in the control or treatment groups at the concentration of 10 μg/mL. Both CFU numbers for inhibition and eradication assays of *Pg* biofilms exhibited complete elimination of biofilms at 50 μg/mL with no observable colonies forming. The above results demonstrated that bismuth particles had promising antibacterial and anti-biofilm effects on the selected Gram-negative oral pathogens.

4. Conclusions

In the present study, we have reported two facile approaches to synthesizing bismuth particles (Ellipsoids and Rods) at micron-scale, and the latter as rod-like bismuth MOFs have been proven to be aligned with the crystalline structure of CAU-17. Notably, we are the first group to demonstrate the crystallization of CAU-17 *via* a two-step process under a stirring-free ambient condition. Remarkably, the bismuth-based particles with low cytotoxicity in human gingival fibroblasts exhibited potent antimicrobial effects on the representative Gram-negative oral pathogens (*A. actinomycetemcomitans* and *P. gingivalis*) in both planktonic and biofilm forms. Compared to CBS, the constructed Bi particles could function as a reservoir of Bi ions for extending the antimicrobial duration. In view of the porous structure and high surface area of MOFs, Rods may serve as a promising multifunctional platform to accommodate small molecules and achieve target delivery for tackling common inflammatory diseases like periodontitis and systemic comorbidities. Importantly, our novel findings may facilitate the precise synthesis of bismuth-based particles
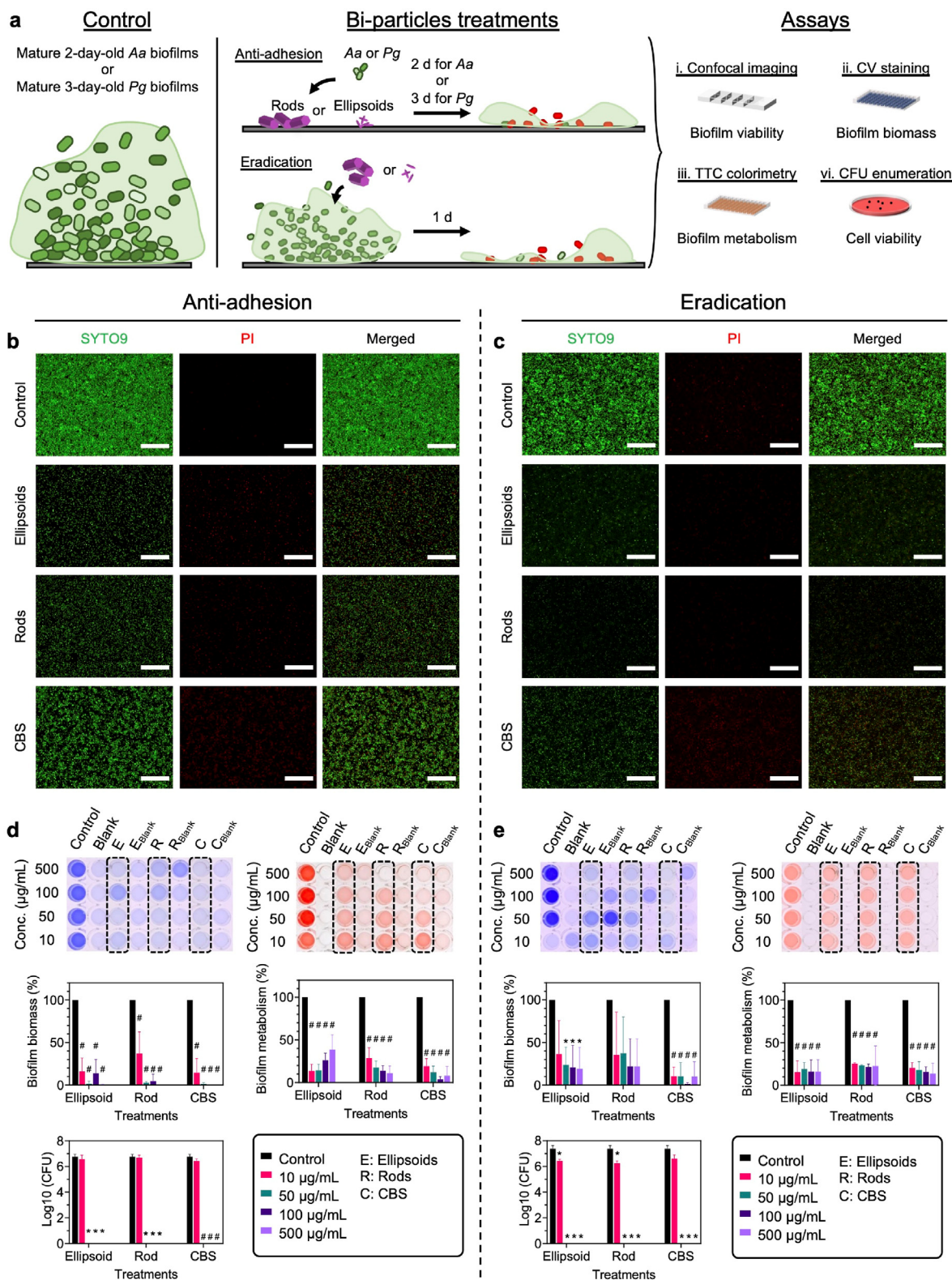
Fig. 9. (a) Illustrative scheme of studying anti-biofilm activities (anti-adhesion and eradication) of Ellipsoids and Rods on *Aa* and *Pg*. *Aa* or *Pg* (1.5×10^7 CFU/mL) was either seeded into the 96-well plates with Ellipsoids, Rods or CBS at different concentrations (500, 100, 50 and 10 μg/mL) and incubated for 2 or 3 d, respectively (anti-adhesion); or statically grown 2 or 3 d to mature state before adding the treatments and further incubated for 1 d (eradication). Confocal imaging, CV biomass staining, TTC metabolism colorimetry and CFU viable cell enumeration were performed to comprehensively evaluate the anti-biofilm effects of Ellipsoids, Rods and CBS. Representative confocal images of *Pg* biofilms treated with Ellipsoids, Rods or CBS at 50 μg/mL for evaluating the (b) anti-adhesion and (c) eradication effects on biofilms (scale bar: 50 μm). Quantitative assays, including CV staining, TTC colorimetry and CFU enumeration, were also conducted to study the (d) anti-adhesion and (e) eradication effects of the as-synthesized Bi particles. The histograms denote the results of three independent tests in duplicate (mean ± SD). The significant differences ($p < 0.05$ or $p < 0.001$) are marked with the asterisk and pound signs, respectively.

and concurrently enrich the applications of the emerging metallic drugs.

Credit authors statement

Funding sources

Declaration of competing interest

The authors declare the following financial interests/personal relationships which may be considered as potential competing interests. Regina Huang, Xuan Li and Lijian Jin have an associated pending patent application related to the current study.

Data availability

Data will be made available on request.

Acknowledgments

Appendix A. Supplementary data

Supplementary data to this article can be found online at https://doi.org/10.1016/j.mtbio.2022.100507.

References

[1] Antimicrobial Resistance Collaborators, Global burden of bacterial antimicrobial resistance in 2019: a systematic analysis, Lancet 399 (2022) 629–655, https://doi.org/10.1016/s0140-6736(21)02724-0.

[2] X. Han, C. Zhao, Z. Pan, X. Tang, Z. Jiang, N-doping of the TiO$_2$/C nanostructure derived from metal-organic frameworks with high drug loading for efficient sonodynamic & chemotherapy, Smart Mater. Med. 3 (2022) 168–178, https://doi.org/10.1016/j.smaim.2022.01.002.

[3] F. Huang, X. Cai, X. Hou, Y. Zhang, J. Liu, L. Yang, Y. Liu, J. Liu, A Dynamic Covalent Polymeric Antimicrobial for Conquering Drug-resistant Bacterial Infection, Exploration, 2022, 20210145, https://doi.org/10.1002/exp.20210145.

[4] Y. Zhou, J. Wu, Y. Li, W. Zhang, Y. Zou, L. Duan, X. Yang, B. Xiao, S. Yi, Fabrication of sulfated silk fibroin-based blend nanofibrous membranes for lysozyme

adsorption, Adv. Fiber Mater. 4 (2022) 89–97, https://doi.org/10.1007/s42765-021-00104-9.

[5] Y. Long, L. Li, T. Xu, X. Wu, Y. Gao, J. Huang, C. He, T. Ma, L. Ma, C. Cheng, C. Zhao, Hedgehog artificial macrophage with atomic-catalytic centers to combat drug-resistant bacteria, Nat. Commun. 12 (2021) 6143, https://doi.org/10.1038/s41467-021-26456-9.

[6] L. Li, S. Cao, Z. Wu, R. Guo, L. Xie, L. Wang, Y. Tang, Q. Li, X. Luo, L. Ma, C. Cheng, L. Qiu, Modulating electron transfer in vanadium-based artificial enzymes for enhanced ROS-catalysis and disinfection, Adv. Mater. 34 (2022), e2108646, https://doi.org/10.1002/adma.202108646.

[7] L. Liu, X. Pan, S. Liu, Y. Hu, D. Ma, Near-infrared light-triggered nitric oxide release combined with low-temperature photothermal therapy for synergetic antibacterial and antifungal, Smart Mater. Med. 2 (2021) 302–313, https://doi.org/10.1016/j.smaim.2021.08.003.

[8] X. Fan, X. Wu, F. Yang, L. Wang, K. Ludwig, L. Ma, A. Trampuz, C. Cheng, R. Haag, A nanohook-equipped bionanocatalyst for localized near-infrared-enhanced catalytic bacterial disinfection, Angew. Chem. Int. Ed. 134 (2022), e202113833, https://doi.org/10.1002/ange.202113833.

[9] M. Tebyetekerwa, Z. Xu, S. Yang, S. Ramakrishna, Electrospun nanofibers-based face masks, Adv. Fiber Mater. 2 (2020) 161–166, https://doi.org/10.1007/s42765-020-00049-5.

[10] J. Zhou, Z. Hu, F. Zabihi, Z. Chen, M. Zhu, Progress and perspective of antiviral protective material, Adv. Fiber Mater. 2 (2020) 123–139, https://doi.org/10.1007/s42765-020-00047-7.

[11] Y. Yang, X. Wu, L. Ma, C. He, S. Cao, Y. Long, J. Huang, R.D. Rodriguez, C. Cheng, C. Zhao, L. Qiu, Bioinspired spiky peroxidase-mimics for localized bacterial capture and synergistic catalytic sterilization, Adv. Mater. 33 (2021), e2005477, https://doi.org/10.1002/adma.202005477.

[12] H.W. Moon, J. Cornella, Bismuth redox catalysis: an emerging main-group platform for organic synthesis, ACS Catal. 12 (2022) 1382–1393, https://doi.org/10.1021/acscatal.1c04897.

[13] F. Li, T. Jiang, J. Zhai, B. Shen, H. Zeng, Exploring novel bismuth-based materials for energy storage applications, J. Mater. Chem. C 6 (2018) 7976–7981, https://doi.org/10.1039/c8tc02801j.

[14] M.A. Shahbazi, L. Faghfouri, M.P.A. Ferreira, P. Figueiredo, H. Maleki, F. Sefat, J. Hirvonen, H.A. Santos, The versatile biomedical applications of bismuth-based nanoparticles and composites: therapeutic, diagnostic, biosensing, and regenerative properties, Chem. Soc. Rev. 49 (2020) 1253–1321, https://doi.org/10.1039/c9cs00283a.

[15] Y. Yang, R. Ouyang, L. Xu, N. Guo, W. Li, K. Feng, L. Ouyang, Z. Yang, S. Zhou, Y. Miao, Review: bismuth complexes: synthesis and applications in biomedicine, J. Coord. Chem. 68 (2015) 379–397, https://doi.org/10.1080/00958972.2014.999672.

[16] C.N. Tsang, K.S. Ho, H.Z. Sun, W.T. Chan, Tracking bismuth antiulcer drug uptake in single *Helicobacter pylori* cells, J. Am. Chem. Soc. 133 (2011) 7355–7357, https://doi.org/10.1021/ja2013278.

[17] T. Deng, Y. Jia, Z. Tong, J. Shi, Z. Wang, Y. Liu, Bismuth drugs reverse Tet(X)-conferred tigecycline resistance in Gram-negative bacteria, Microbiol. Spectr. 10 (2022), e0157821, https://doi.org/10.1128/spectrum.01578-21.

[18] R. Wang, T.P. Lai, P. Gao, H. Zhang, P.L. Ho, P.C. Woo, G. Ma, R.Y. Kao, H. Li, H.Z. Sun, Bismuth antimicrobial drugs serve as broad-spectrum metallo-beta-lactamase inhibitors, Nat. Commun. 9 (2018) 439, https://doi.org/10.1038/s41467-018-02828-6.

[19] C. Wang, X. Li, T. Cheng, H. Sun, L. Jin, Eradication of *Porphyromonas gingivalis* persisters through colloidal bismuth subcitrate synergistically combined with metronidazole, Front. Microbiol. 12 (2021), 748121, https://doi.org/10.3389/fmicb.2021.748121.

[20] T.F. Cheng, Y.T. Lai, C. Wang, Y. Wang, N. Jiang, H. Li, H.Z. Sun, L.J. Jin, Bismuth drugs tackle *Porphyromonas gingivalis* and attune cytokine response in human cells, Metallomics 11 (2019) 1207–1218, https://doi.org/10.1039/c9mt00085b.

[21] S. Yuan, R. Wang, J.F. Chan, A.J. Zhang, T.F. Cheng, K.K. Chik, Z.W. Ye, S. Wang, A.C. Lee, L.J. Jin, H. Li, D.Y. Jin, K.Y. Yuen, H.Z. Sun, Metallodrug ranitidine bismuth citrate suppresses SARS-CoV-2 replication and relieves virus-associated pneumonia in Syrian hamsters, Nat. Microbiol. 5 (2020) 1439–1448, https://doi.org/10.1038/s41564-020-00802-x.

[22] R. Wang, J.F.-W. Chan, S. Wang, H. Li, J. Zhao, T.K.-Y. Ip, Z. Zuo, K.-Y. Yuen, S. Yuan, H.Z. Sun, Orally administered bismuth drug together with *N*-acetyl cysteine as a broad-spectrum anti-coronavirus cocktail therapy, Chem. Sci. 13 (2022) 2238–2248, https://doi.org/10.1039/d1sc04515f.

[23] D.M. Griffith, H. Li, M.V. Werrett, P.C. Andrews, H.Z. Sun, Medicinal chemistry and biomedical applications of bismuth-based compounds and nanoparticles, Chem. Soc. Rev. 50 (2021) 12037–12069, https://doi.org/10.1039/d0cs00031k.

[24] N. Motakef-Kazemi, M. Yaqoubi, Green synthesis and characterization of bismuth oxide nanoparticle using *Mentha pulegium* extract, Iran, J. Pharmacol. Sci. 19 (2020) 70–79, https://doi.org/10.22037/ijpr.2019.15578.13190.

[25] X. Yu, A. Li, C. Zhao, K. Yang, X. Chen, W. Li, Ultrasmall semimetal nanoparticles of bismuth for dual-modal computed tomography/photoacoustic imaging and synergistic thermoradiotherapy, ACS Nano 11 (2017) 3990–4001, https://doi.org/10.1021/acsnano.7b00476.

[26] M. Bartoli, P. Jagdale, A. Tagliaferro, A short review on biomedical applications of nanostructured bismuth oxide and related nanomaterials, Materials 13 (2020) 5234, https://doi.org/10.3390/ma13225234.

[27] C. Gomez, G. Hallot, S. Laurent, M. Port, Medical applications of metallic bismuth nanoparticles, Pharmaceutics 13 (2021) 1793, https://doi.org/10.3390/pharmaceutics13111793.

[28] Q.-X. Wang, G. Li, Bi(iii) MOFs: syntheses, structures and applications, Inorg. Chem. Front. 8 (2021) 572–589, https://doi.org/10.1039/d0qi01055c.

[29] Q.L. Zhu, Q. Xu, Metal-organic framework composites, Chem. Soc. Rev. 43 (2014) 5468–5512, https://doi.org/10.1039/c3cs60472a.

[30] M. Zhao, Y. Huang, Y. Peng, Z. Huang, Q. Ma, H. Zhang, Two-dimensional metal-organic framework nanosheets: synthesis and applications, Chem. Soc. Rev. 47 (2018) 6267–6295, https://doi.org/10.1039/c8cs00268a.

[31] Y.-R. Lee, J. Kim, W.-S. Ahn, Synthesis of metal-organic frameworks: a mini review, Kor. J. Chem. Eng. 30 (2013) 1667–1680, https://doi.org/10.1007/s11814-013-0140-6.

[32] S.L. Griffin, N.R. Champness, A periodic table of metal-organic frameworks, Coord. Chem. Rev. 414 (2020), https://doi.org/10.1016/j.ccr.2020.213295.

[33] W. Xuan, C. Zhu, Y. Liu, Y. Cui, Mesoporous metal-organic framework materials, Chem. Soc. Rev. 41 (2012) 1677–1695, https://doi.org/10.1039/c1cs15196g.

[34] P. Horcajada, R. Gref, T. Baati, P.K. Allan, G. Maurin, P. Couvreur, G. Ferey, R.E. Morris, C. Serre, Metal-organic frameworks in biomedicine, Chem. Rev. 112 (2012) 1232–1268, https://doi.org/10.1021/cr200256v.

[35] J. Liu, L. Chen, H. Cui, J. Zhang, L. Zhang, C.Y. Su, Applications of metal-organic frameworks in heterogeneous supramolecular catalysis, Chem. Soc. Rev. 43 (2014) 6011–6061, https://doi.org/10.1039/c4cs00094c.

[36] D. Liu, D. Zou, H. Zhu, J. Zhang, Mesoporous metal-organic frameworks: synthetic strategies and emerging applications, Small 14 (2018), e1801454, https://doi.org/10.1002/smll.201801454.

[37] Y.H. Cheung, K. Ma, H.C. van Leeuwen, M.C. Wasson, X. Wang, K.B. Idrees, W. Gong, R. Cao, J.J. Mahle, T. Islamoglu, G.W. Peterson, M.C. de Koning, J.H. Xin, O.K. Farha, Immobilized regenerable active chlorine within a zirconium-based MOF textile composite to eliminate biological and chemical threats, J. Am. Chem. Soc. 143 (2021) 16777–16785, https://doi.org/10.1021/jacs.1c08576.

[38] L.J. Murray, M. Dinca, J.R. Long, Hydrogen storage in metal-organic frameworks, Chem. Soc. Rev. 38 (2009) 1294–1314, https://doi.org/10.1039/b802256a.

[39] X. Fan, F. Yang, J. Huang, Y. Yang, C. Nie, W. Zhao, L. Ma, C. Cheng, C. Zhao, R. Haag, Metal–organic-framework-derived 2D carbon nanosheets for localized multiple bacterial eradication and augmented anti-infective therapy, Nano Lett. 19 (2019) 5885–5896, https://doi.org/10.1021/acs.nanolett.9b01400.

[40] M. Köppen, O. Beyer, S. Wuttke, U. Luning, N. Stock, Synthesis, functionalisation and post-synthetic modification of bismuth metal-organic frameworks, Dalton Trans. 46 (2017) 8658–8663, https://doi.org/10.1039/c7dt01744h.

[41] S. Iram, M. Imran, F. Kanwal, Z. Iqbal, F. Deeba, Q.J. Iqbal, Bismuth(III) based metal organic framework: luminescence, gas adsorption, and antibacterial studies, Z. fur Anorg. Allg. Chem. 645 (2019) 50–56, https://doi.org/10.1002/zaac.201800383.

[42] Q.L. Guan, C. Han, F.Y. Bai, J. Liu, Y.H. Xing, Z. Shi, L.X. Sun, Bismuth-MOF based on tetraphenylethylene derivative as a luminescent sensor with turn-off/on for application of Fe^{3+} detection in serum and bioimaging, as well as emissive spectra analysis by TRES, Sensor. Actuator. B Chem. 325 (2020), 128767, https://doi.org/10.1016/j.snb.2020.128767.

[43] E.S. Grape, J.G. Flores, T. Hidalgo, E. Martinez-Ahumada, A. Gutierrez-Alejandre, A. Hautier, D.R. Williams, M. O'Keeffe, L. Ohrstrom, T. Willhammar, P. Horcajada, I.A. Ibarra, A.K. Inge, A robust and biocompatible bismuth ellagate MOF synthesized under green ambient conditions, J. Am. Chem. Soc. 142 (2020) 16795–16804, https://doi.org/10.1021/jacs.0c07525.

[44] M. Köppen, A. Dhakshinamoorthy, A.K. Inge, O. Cheung, J. Ångström, P. Mayer, N. Stock, Synthesis, transformation, catalysis, and gas sorption investigations on the bismuth metal–organic framework CAU-17, Eur. J. Inorg. Chem. (2018) 3496–3503, https://doi.org/10.1002/ejic.201800321, 2018.

[45] M. Feyand, E. Mugnaioli, F. Vermoortele, B. Bueken, J.M. Dieterich, T. Reimer, U. Kolb, D. de Vos, N. Stock, Automated diffraction tomography for the structure elucidation of twinned, sub-micrometer crystals of a highly porous, catalytically active bismuth metal-organic framework, Angew. Chem. Int. Ed. 51 (2012) 10373–10376, https://doi.org/10.1002/anie.201204963.

[46] M. Song, Y. Liu, X. Huang, S. Ding, Y. Huang, J. Shen, K. Zhu, A broad-spectrum antibiotic adjuvant reverses multidrug-resistant Gram-negative pathogens, Nat. Microbiol. 5 (2020) 1040–1050, https://doi.org/10.1038/s41564-020-0723-z.

[47] V. Di Onofrio, R. Gesuele, A. Maione, G. Liguori, R. Liguori, M. Guida, R. Nigro, E. Galdiero, Prevention of *Pseudomonas aeruginosa* biofilm formation on soft contact lenses by *Allium sativum* fermented extract (BGE) and cannabinol oil extract (CBD), Antibiotics 8 (2019) 258, https://doi.org/10.3390/antibiotics8040258.

[48] J.H. Merritt, D.E. Kadouri, G.A. O'Toole, Growing and analyzing static biofilms (Chapter 1), Curr. Protoc. Microbiol. (2005), https://doi.org/10.1002/9780471729259.mc01b01s00. Unit 1B 1.

[49] E. Ploetz, A. Zimpel, V. Cauda, D. Bauer, D.C. Lamb, C. Haisch, S. Zahler, A.M. Vollmar, S. Wuttke, H. Engelke, Metal–organic framework nanoparticles induce pyroptosis in cells controlled by the extracellular pH, Adv. Mater. 32 (2020), 1907267, https://doi.org/10.1002/adma.201907267.

[50] H. Reinsch, Green" synthesis of metal-organic frameworks, Eur. J. Inorg. Chem. (2016) 4290–4299, https://doi.org/10.1002/ejic.201600286, 2016.

[51] J. Xu, J. Liu, Z. Li, X. Wang, Y. Xu, S. Chen, Z. Wang, Optimized synthesis of Zr^{iv} metal organic frameworks (MOFs-808) for efficient hydrogen storage, New J. Chem. 43 (2019) 4092–4099, https://doi.org/10.1039/c8nj06362a.

[52] M. Lv, D.W. Sun, L. Huang, H. Pu, Precision release systems of food bioactive compounds based on metal-organic frameworks: synthesis, mechanisms and recent applications, Crit. Rev. Food Sci. Nutr. (2021) 1–19, https://doi.org/10.1080/10408398.2021.2004086.

[53] V.H. Nguyen, L. Van Tan, T. Lee, T.D. Nguyen, Solvothermal synthesis and photocatalytic activity of metal-organic framework materials based on bismuth and trimesic acid, Sustain. Chem. Pharm. 20 (2021), 100385, https://doi.org/10.1016/j.scp.2021.100385.

[54] G. Wang, Y. Liu, B. Huang, X. Qin, X. Zhang, Y. Dai, A novel metal-organic framework based on bismuth and trimesic acid: synthesis, structure and properties, Dalton Trans. 44 (2015) 16238–16241, https://doi.org/10.1039/c5dt03111g.

[55] C. Vaitsis, G. Sourkouni, C. Argirusis, Metal organic frameworks (MOFs) and ultrasound: a review, Ultrason. Sonochem. 52 (2019) 106–119, https://doi.org/10.1016/j.ultsonch.2018.11.004.

[56] Y. Ying, B. Khezri, J. Kosina, M. Pumera, Reconstructed bismuth-based metal-organic framework nanofibers for selective CO_2-to-formate conversion: morphology engineering, ChemSusChem 14 (2021) 3402–3412, https://doi.org/10.1002/cssc.202101122.

[57] T.D. Bennett, A.K. Cheetham, Amorphous metal-organic frameworks, Acc. Chem. Res. 47 (2014) 1555–1562, https://doi.org/10.1021/ar5000314.

[58] X. Zhang, Y. Zhang, Q. Li, X. Zhou, Q. Li, Y. Yi, Y. Liu, J. Zhang, Highly efficient and durable aqueous electrocatalytic reduction of CO_2 to HCOOH with a novel bismuth–MOF: experimental and DFT studies, J. Mater. Chem. A 8 (2020) 9776–9787, https://doi.org/10.1039/d0ta00384k.

[59] M. Köppen, V. Meyer, J. Ångström, A.K. Inge, N. Stock, Solvent-dependent formation of three new Bi-metal–organic frameworks using a tetracarboxylic acid, Cryst. Growth Des. 18 (2018) 4060–4067, https://doi.org/10.1021/acs.cgd.8b00439.

[60] M. Thommes, K. Kaneko, A.V. Neimark, J.P. Olivier, F. Rodriguez-Reinoso, J. Rouquerol, K.S.W. Sing, Physisorption of gases, with special reference to the evaluation of surface area and pore size distribution (IUPAC Technical Report), Pure Appl. Chem. 87 (2015) 1051–1069, https://doi.org/10.1515/pac-2014-1117.

[61] K.A. Cychosz, M. Thommes, Progress in the physisorption characterization of nanoporous gas storage materials, Engineering 4 (2018) 559–566, https://doi.org/10.1016/j.eng.2018.06.001.

[62] S.-R. Zhu, M.-K. Wu, W.-N. Zhao, P.-F. Liu, F.-Y. Yi, G.-C. Li, K. Tao, L. Han, In situ growth of metal–organic framework on BiOBr 2D material with excellent photocatalytic activity for dye degradation, Cryst. Growth Des. 17 (2017) 2309–2313, https://doi.org/10.1021/acs.cgd.6b01811.

[63] J. Rodriguez-Pereira, S.A. Rincón-Ortiz, R. Ospina, Bismuth acetate by XPS, Surf. Sci. Spectra 27 (2020), 024001, https://doi.org/10.1116/6.0000270.

[64] H. Ouyang, N. Chen, G. Chang, X. Zhao, Y. Sun, S. Chen, H. Zhang, D. Yang, Selective capture of toxic selenite anions by bismuth-based metal-organic frameworks, Angew. Chem. Int. Ed. 57 (2018) 13197–13201, https://doi.org/10.1002/anie.201807891.

[65] D. Yao, C. Tang, L. Li, B. Xia, A. Vasileff, H. Jin, Y. Zhang, S.Z. Qiao, In situ fragmented bismuth nanoparticles for electrocatalytic nitrogen reduction, Adv. Energy Mater. 10 (2020), 2001289, https://doi.org/10.1002/aenm.202001289.

[66] L. Xu, Y. Xu, X. Li, Z. Wang, T. Sun, X. Zhang, Eu(3+)/Tb(3+) functionalized Bi-based metal-organic frameworks toward tunable white-light emission and fluorescence sensing applications, Dalton Trans. 47 (2018) 16696–16703, https://doi.org/10.1039/c8dt03474e.

[67] N. Stock, S. Biswas, Synthesis of metal-organic frameworks (MOFs): routes to various MOF topologies, morphologies, and composites, Chem. Rev. 112 (2012) 933–969, https://doi.org/10.1021/cr200304e.

[68] M.J. Van Vleet, T. Weng, X. Li, J.R. Schmidt, In situ, time-resolved, and mechanistic studies of metal-organic framework nucleation and growth, Chem. Rev. 118 (2018) 3681–3721, https://doi.org/10.1021/acs.chemrev.7b00582.

[69] M. Taheri, D. Ashok, T. Sen, T.G. Enge, N.K. Verma, A. Tricoli, A. Lowe, D.R. Nisbet, T. Tsuzuki, Stability of ZIF-8 nanopowders in bacterial culture media and its implication for antibacterial properties, Chem. Eng. J. 413 (2021), 127511, https://doi.org/10.1016/j.cej.2020.127511.

[70] C. Orellana-Tavra, M. Koppen, A. Li, N. Stock, D. Fairen-Jimenez, Biocompatible, crystalline, and amorphous bismuth-based metal-organic frameworks for drug delivery, ACS Appl. Mater. Interfaces 12 (2020) 5633–5641, https://doi.org/10.1021/acsami.9b21692.

[71] D. Cunha, M. Ben Yahia, S. Hall, S.R. Miller, H. Chevreau, E. Elkaïm, G. Maurin, P. Horcajada, C. Serre, Rationale of drug encapsulation and release from biocompatible porous metal–organic frameworks, Chem. Mater. 25 (2013) 2767–2776, https://doi.org/10.1021/cm400798p.

[72] M. Kuboniwa, R.J. Lamont, Subgingival biofilm formation, Periodontol. 2000 52 (2010) 38–52, https://doi.org/10.1111/j.1600-0757.2009.00311.x.

[73] M. Shen, F. Forghani, X. Kong, D. Liu, X. Ye, S. Chen, T. Ding, Antibacterial applications of metal-organic frameworks and their composites, Compr. Rev. Food Sci. Food Saf. 19 (2020) 1397–1419, https://doi.org/10.1111/1541-4337.12515.

[74] A. Hrioua, A. Loudiki, A. Farahi, F. Laghrib, M. Bakasse, S. Lahrich, S. Saqrane, M.A. El Mhammedi, Complexation of amoxicillin by transition metals: physico-chemical and antibacterial activity evaluation, Bioelectrochemistry 142 (2021), 107936, https://doi.org/10.1016/j.bioelechem.2021.107936.

[75] N. Bhardwaj, S.K. Pandey, J. Mehta, S.K. Bhardwaj, K.H. Kim, A. Deep, Bioactive nano-metal-organic frameworks as antimicrobials against Gram-positive and Gram-negative bacteria, Toxicol. Res. 7 (2018) 931–941, https://doi.org/10.1039/c8tx00087e.

[76] G. Wyszogrodzka, B. Marszalek, B. Gil, P. Dorozynski, Metal-organic frameworks: mechanisms of antibacterial action and potential applications, Drug Discov. Today 21 (2016) 1009–1018, https://doi.org/10.1016/j.drudis.2016.04.009.

[77] C.T. Huang, P.S. Stewart, Reduction of polysaccharide production in *Pseudomonas aeruginosa* biofilms by bismuth dimercaprol (BisBAL) treatment, J. Antimicrob. Chemother. 44 (1999) 601–605, https://doi.org/10.1093/jac/44.5.601.

[78] P. Domenico, J.M. Tomas, S. Merino, X. Rubires, B.A. Cunha, Bismuth-dimercaprol exposes surface components of *Klebsiella pneumoniae* camouflaged by the polysaccharide capsule, Ann. NY Acad. Sci. 797 (1996) 269–270, https://doi.org/10.1111/j.1749-6632.1996.tb52974.x.

[79] A.L. Vega-Jimenez, A. Almaguer-Flores, M. Flores-Castaneda, E. Camps, M. Uribe-Ramirez, O.G. Aztatzi-Aguilar, A. De Vizcaya-Ruiz, Bismuth subsalicylate nanoparticles with anaerobic antibacterial activity for dental applications, Nanotechnology 28 (2017), 435101, https://doi.org/10.1088/1361-6528/aa8838.

[80] B. Han, Z. Zhang, Y. Xie, X. Hu, H. Wang, W. Xia, Y. Wang, H. Li, Y. Wang, H. Sun, Multi-omics and temporal dynamics profiling reveal disruption of central metabolism in *Helicobacter pylori* on bismuth treatment, Chem. Sci. 9 (2018) 7488–7497, https://doi.org/10.1039/c8sc01668b.

[81] A. Yoshida, M. Yoshimura, N. Ohara, S. Yoshimura, S. Nagashima, T. Takehara, K. Nakayama, Hydrogen sulfide production from cysteine and homocysteine by periodontal and oral bacteria, J. Periodontol. 80 (2009) 1845–1851, https://doi.org/10.1902/jop.2009.090012.

[82] R. Pianotti, S. Lachette, S. Dills, Desulfuration of cysteine and methionine by *Fusobacterium nucleatum*, J. Dent. Res. 65 (1986) 913–917, https://doi.org/10.1177/00220345860650061101.

[83] K. Shatalin, A. Nuthanakanti, A. Kaushik, D. Shishov, A. Peselis, I. Shamovsky, B. Pani, M. Lechpammer, N. Vasilyev, E. Shatalina, D. Rebatchouk, A. Mironov, P. Fedichev, A. Serganov, E. Nudler, Inhibitors of bacterial H₂S biogenesis targeting antibiotic resistance and tolerance, Science 372 (2021) 1169–1175, https://doi.org/10.1126/science.abd8377.

[84] L. Luhachack, E. Nudler, Bacterial gasotransmitters: an innate defense against antibiotics, Curr. Opin. Microbiol. 21 (2014) 13–17, https://doi.org/10.1016/j.mib.2014.06.017.

[85] K. Shatalin, E. Shatalina, A. Mironov, E. Nudler, H₂S: a universal defense against antibiotics in bacteria, Science 334 (2011) 986–990, https://doi.org/10.1126/science.1209855.

[86] J.P. Motta, J.L. Wallace, A.G. Buret, C. Deraison, N. Vergnolle, Gastrointestinal biofilms in health and disease, Nat. Rev. Gastroenterol. Hepatol. 18 (2021) 314–334, https://doi.org/10.1038/s41575-020-00397-y.

[87] H.C. Flemming, S. Wuertz, Bacteria and archaea on Earth and their abundance in biofilms, Nat. Rev. Microbiol. 17 (2019) 247–260, https://doi.org/10.1038/s41579-019-0158-9.

[88] J.F. Lasserre, M.C. Brecx, S. Toma, Oral microbes, biofilms and their role in periodontal and peri-implant diseases, Materials 11 (2018) 1802, https://doi.org/10.3390/ma11101802.

[89] J.W. Costerton, P.S. Stewart, E.P. Greenberg, Bacterial biofilms: a common cause of persistent infections, Science 284 (1999) 1318–1322, https://doi.org/10.1126/science.284.5418.1318.

[90] T. Okuda, E. Kokubu, T. Kawana, A. Saito, K. Okuda, K. Ishihara, Synergy in biofilm formation between *Fusobacterium nucleatum* and *Prevotella* species, Anaerobe 18 (2012) 110–116, https://doi.org/10.1016/j.anaerobe.2011.09.003.

[91] Y. Saito, R. Fujii, K.I. Nakagawa, H.K. Kuramitsu, K. Okuda, K. Ishihara, Stimulation of *Fusobacterium nucleatum* biofilm formation by *Porphyromonas gingivalis*, Oral Microbiol. Immunol. 23 (2008) 1–6, https://doi.org/10.1111/j.1399-302X.2007.00380.x.

[92] S. Kamiloglu, G. Sari, T. Ozdal, E. Capanoglu, Guidelines for cell viability assays, Food Frontiers 1 (2020) 332–349, https://doi.org/10.1002/fft2.44.

[93] Y. Qiao, L. Ma, Quantification of metal ion induced DNA damage with single cell array based assay, Analyst 138 (2013) 5713–5718, https://doi.org/10.1039/c3an00967j.

[94] C.D. Boswell, C.J. Hewitt, L.E. Macaskie, An application of bacterial flow cytometry: evaluation of the toxic effects of four heavy metals on *Acinetobacter* sp. with potential for bioremediation of contaminated wastewaters, Biotechnol. Lett. 20 (1998) 857–863, https://doi.org/10.1023/a:1005363525882.

[95] J.P. Lewis, Metal uptake in host-pathogen interactions: role of iron in *Porphyromonas gingivalis* interactions with host organisms, Periodontol. 2000 52 (2010) 94–116, https://doi.org/10.1111/j.1600-0757.2009.00329.x.

[96] M. Berney, F. Hammes, F. Bosshard, H.U. Weilenmann, T. Egli, Assessment and interpretation of bacterial viability by using the LIVE/DEAD BacLight Kit in combination with flow cytometry, Appl. Environ. Microbiol. 73 (2007) 3283–3290, https://doi.org/10.1128/AEM.02750-06.